Sub-Maximal Exchange Flow over a Sill with Barotropic Forcing

by

Ryan Clouston
B.SC., University of Victoria, 2010

A Thesis Submitted in Partial Fulfillment of the
Requirements for the Degree of

MASTER OF SCIENCE

in the School of Earth and Ocean Sciences

Sub-Maximal Exchange Flow over a Sill with Barotropic Forcing

by

Ryan Clouston
B.SC., University of Victoria, 2010

Supervisory Committee

Dr. Jody Klymak, Supervisor
(School of Earth and Ocean Sciences)

Dr. Adam Monahan, Departmental Member
(School of Earth and Ocean Sciences)

Dr. David Farmer, Outside Member
(School of Earth and Ocean Sciences)

Supervisory Committee

Dr. Jody Klymak, Supervisor
(School of Earth and Ocean Sciences)

Dr. Adam Monahan, Departmental Member
(School of Earth and Ocean Sciences)

Dr. David Farmer, Outside Member
(School of Earth and Ocean Sciences)

ABSTRACT

Two basins separated by a strait often have different densities due to environmental factors, resulting in a situation in the strait where fluids of different densities are essentially side-by-side, causing an exchange flow due to gravitational forces. Dense fluid is pulled below light fluid and the light fluid is pushed above the dense, creating an opposing flow in the two layers. This exchange is often "controlled" at the point in the strait where cross-sectional area is minimized due to a constriction, either horizontal or vertical.

Exchange in the strait can control the dynamics, and in turn energy, nutrient, pollutant and biological transport between the basins. Since strait dynamics are often not resolved in regional or global models, it is useful to parameterize the exchange based on external variables such as the density difference in the basins, the level of the dense water in the dense basin, and the tidal forcing.

Exchange flow can be "maximal" or "sub-maximal". The flow is "maximal" if raising the interface in the dense basin (presumably by modifying light water to be dense) does not further increase the exchange flow through the strait. While many ocean straits are usually "maximal", there are also many that are "sub-maximal," and thus require separate theoretical treatment.

Time-dependent external barotropic forcing (i.e. the tide) modifies the time-averaged exchange flow in a strait. The relationship between tidal forcing and the average exchange flow in a channel has been examined for maximal exchange (Helfrich, 1995). In the present study, that effort is extended to include tidal forcing on a sub-maximal exchange flow. A strait with a sill is simulated numerically, using a two layer hydrostatic approximation. Time-averaged exchange flow increases with tidal amplitude depending on three factors: the physical dimensions of the problem, the tidal amplitude, and the relative strength of flow of the density layers.

Results show that all exchange flows increase at a similar rate with tidal forcing, after being normalized by a parameter relating physical dimensions of the strait to the interfacial wave speed. This result quantifies the exchange increase due to tidal forcing for all degrees of "maximality" in this simple sill-only geometry. This relates time-dependent sub-maximal flows to the maximal case that has already been studied in depth.

Contents

List of Figures

ACKNOWLEDGEMENTS

I would like to thank:

My friends and family, for supporting me in the low moments.

Jody Klymak, for mentoring, support, encouragement, and patience.

Chapter 1

Introduction

The ability to model exchange flow of all kinds has implications for studying and understanding large and small scale strait dynamics. Large scale exchange flows, such as in the Red Sea (Pratt et al., 1999), the Mediterranean Sea (Wesson and Gregg, 1994), and the Strait of Gibraltar (Bray et al., 1995) can affect local to global systems. Internal waves and solitons created due to tidal interactions with these flows have been observed in many areas and are significant sources of energy. The salinity budget of the Mediterranean basin is controlled by the exchange flow of the Strait of Gibraltar (Bray et al., 1995), whose outflow has been detected across the North Atlantic (Frankcombe and Hogg, 2007). Large scale ocean and climate models have difficulty resolving strait dynamics, so it is important to be able to predict the exchange from basin-scale parameters.

Exchange flows are also important on a regional scale, such as in estuaries or lagoons connected to coastal oceans. Exchange affects the ecology, residence time, water quality and salinity budgets of the basins. Pollutant concentrations due to discharge into connected basins depend on the exchange flow. For example, if a sewage treatment plant releases its outflow into a basin that flows into an estuary, the ongoing transport of its waste towards the ocean depends on the exchange flow. Similarly, nutrient concentrations in the basins rely on the exchange. Dense water that pools at the bottom of the fresh basin can harbour life, as these waters are often rich in nutrients. The continued productivity depends on the renewal of these nutrients by the exchange flow, and thus the life cycle of some fjords such as the Saanich Inlet can rely on the activity of exchange flows (Manning et al., 2010). The oxygen concentration is a critical variable affecting biology in Saanich Inlet, and it depends on the deep water exchange flow. Changes in surface flow due to exchange flows can also affect ship traffic through these straits, particularly neutrally buoyant ships (i.e. submarines).

Two isolated reservoirs separated by a strait often have different densities due to environmental factors. These will be known as the “light reservoir” and the “dense reservoir”. Exchange flows are often observed naturally where freshwater sources such as estuaries, fjords, and rivers meet more dense waters, such as cold and salty waters from seas and oceans. The exchange between these waters can often be approximated as a two-layer exchange flow, with a fresh layer outflow and a dense layer inflow. An example from Knight Inlet shows the process, though it also makes clear that simplifying the exchange flow into two layers is not always accurate (Figure 1.1). Gravity pulls dense fluid below lighter fluids, generating exchange flow in the strait connecting these basins. The exchange occurs in the absence of any exterior forcing, and here we will call this “gravitational flow” due to “gravitational forcing”.

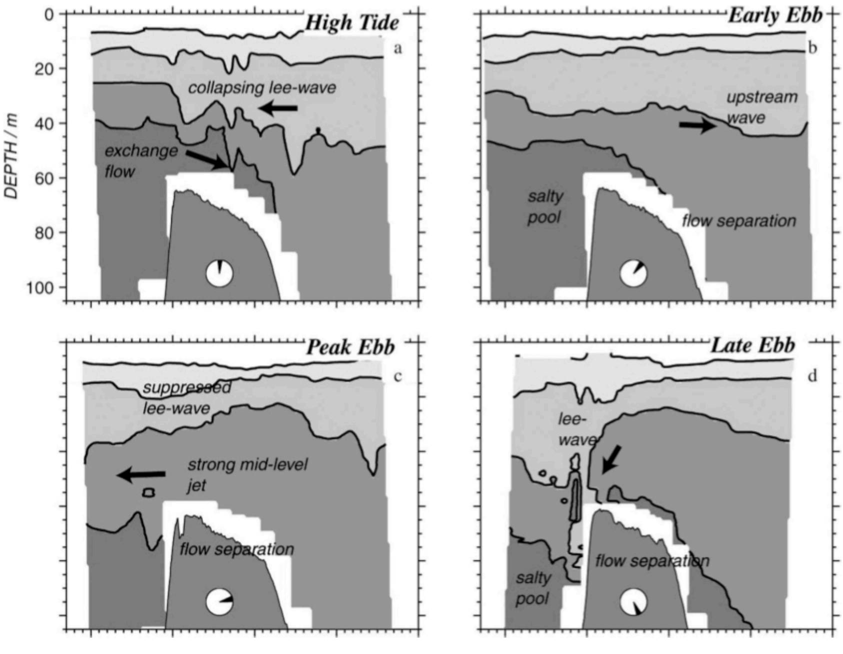

FIG. 16. Summary of the response during ebb tide. Isopycnals are from the data and are contoured at σ_θ = 17, 23, 24, 24.25 kg m^{-3}.

Figure 1.1: Tidally induced exchange flow at Knight Inlet. The dense water layer only flows over the sill at High Tide, showing how important tidal flow is to this sub-maximal exchange flow. Leeward water is pumped over the sill each flood tide and suppressed each ebb. (Klymak and Gregg, 2003)

Two-layer exchange has been studied in great depth for the case of “maximal” exchange flow, largely due to its application to the strait of Gibraltar, thought to be maximal (Farmer and Armi, 1986; Helfrich, 1995). Maximal exchange is the steady-state maximum volumetric flow rate that exists for the physical dimensions of the channel. This gravitational flow is called “maximal” when the level of the dense fluid in the dense reservoir is high, and raising it higher does not increase the exchange flow.

While maximal exchange has been studied in depth, it is only a special case of exchange between two basins. If the level of the dense fluid is lower than the maximal level, then the exchange is weaker than maximal, and termed “sub-maximal”. In Figure 1.2 three different levels of gravitational forcing are displayed in a strait of constant width, defined by h_1, the thickness of the light layer far to the right of the sill as a fraction of the depth of the sill crest. These cases are maximal ($h_1 = 0.3694$), sub-maximal ($h_1 = 0.6234$), and greatly sub-maximal (almost blocked; $h_1 = 0.9868$). As h_1 increases, the exchange flow, q_{is}, decreases, as the interface in the dense basin drops.

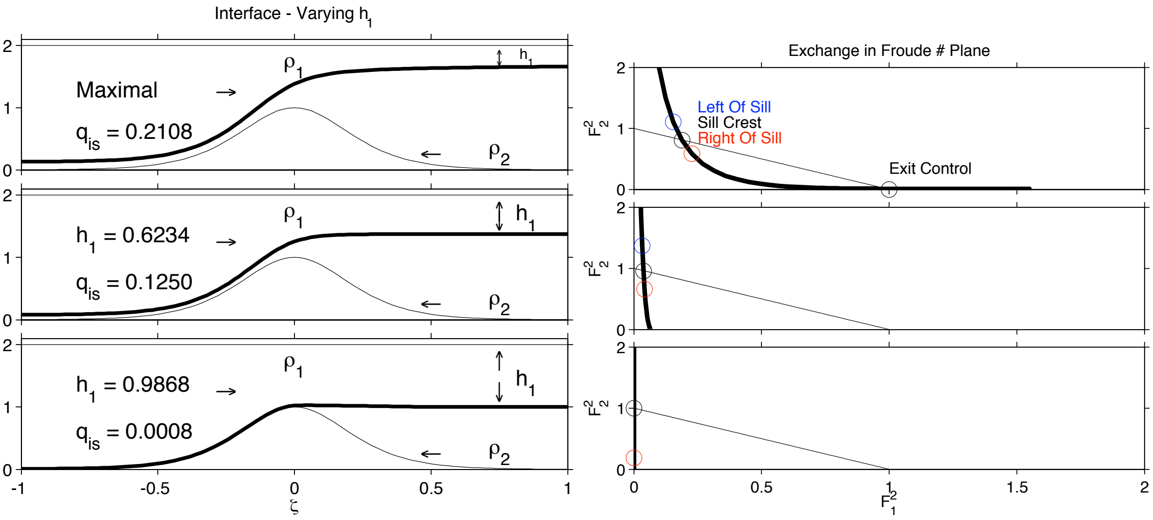

Figure 1.2: On the left, steady interface plots for three cases of varying h_1 are displayed, from maximal (top) to extremely sub-maximal (bottom). q_{is} is the steady state exchange flow, and decreases as h_1 increases. $\zeta = \frac{x}{L}$, where L is a length scale of the strait. Arrows show the direction of flow in the density layers. To the right of each interface plot is the representation of the exchange in the Froude-Number plane. The thin line represents $G^2 = 1$, the definition of criticality. The blue and red circles represents the points at which $\zeta = -0.02$ and $\zeta = 0.02$ respectively.

In order to describe the hydraulic control of the exchange flow imposed by constrictions, the concept of 'criticality' is used (Armi, 1986; Farmer and Armi, 1986). A dimensionless value called the Froude number, F, quantifies the hydraulic state of single layer flow:

$$F_i = \frac{u_i}{\sqrt{g' y_i}} \tag{1.1}$$

This represents the fluid speed as a fraction of the significant wave speed in the channel. Here, u_i is layer velocity, h_i is the layer thickness, and subscript i is the layer index. In this study, i=1 represents the lighter top layer, and i=2 is the dense bottom layer (Figure 1.3). g' represents the reduced gravitational acceleration of the interface between the layers:

$$g' = \frac{g \Delta\rho}{\rho_2} \tag{1.2}$$

where g is gravitational acceleration, $\Delta\rho = \rho_2 - \rho_1$ is the difference between layer densities, and ρ_2 is the lower layer density.

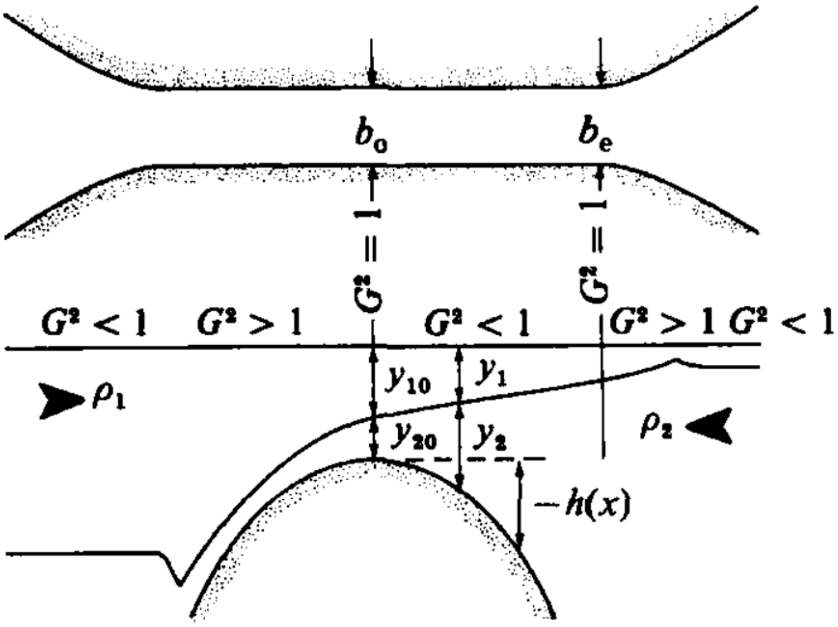

Figure 1.3: Physical representation of the model (Farmer and Armi, 1986). In the current project, $b(x)$ is kept constant.

For two-layer steady exchange flow, the composite Froude number G^2 describes the flow;

$$G^2 = F_1^2 + F_2^2 = \frac{u_1^2}{g' y_1} + \frac{u_2^2}{g' y_2} \tag{1.3}$$

G^2 represents the mean fluid speed among layers as a fraction of the relevant fastest internal wave speed in the channel. The internal wave speed depends on the cross-sectional area of the flow, thus each cross-section has a single composite Froude number. Similarly to F_i, the value of G^2 demonstrates the sub-critical, critical, and supercritical conditions of the two-layer exchange flow. When $G^2 = 1$, flow is critical, when below this value flow is sub-critical, and when above $G^2 = 1$ flow is supercritical.

The use of these terms is illustrated in Figure 1.2. The interface depth as the flow crosses a sill is shown in the left side, while the right hand plots indicate the Froude numbers. For all three cases the flow to the right of the sill is sub-critical, with $G^2 < 1$, transiting to critical at the crest, and supercritical as the dense layer descends along the lee face of the sill (Figure 1.3). The reservoir condition in the light basin is such that the dense layer remains supercritical, although if a reservoir of dense water exists at some depth in this basin, the descending dense flow would eventually have to match this ‘downstream condition’. This might occur, for example, via hydraulic jump, transitioning the flow back to subcritical (Baines, 1995). Note that the sub-maximal flows are much “steeper” in the Froude number plane because the thick upper layer always stays very subcritical.

Thus far only steady exchange flows have been mentioned. However, in exchange flows such as Knight Inlet (Figure 1.1) and Gibraltar, tidal forcing is important, and periodic flow reversals are observed. Barotropic forcing, either steady or time-dependent, can be categorized in terms of its overall effect on the flow. For steady barotropic flow, “moderate” forcing varies the exchange rate from the steady case, but still allows for two layers to exist flowing in opposite directions (Baines, 1995). “Strong” forcing can arrest the flow of one layer at the narrows. “Intermediate” forcing allows both layers to exist at the narrows, but causes one of these layers to remain stationary. Time-dependent exchange flows vary between these categories.

Exchange flow has traditionally been studied using steady hydraulic theory, assuming the flow can be thought of as steady in time, or as a sequence of steady states. This may not apply in some tidal regimes, however some general effects barotropic forcing has on exchange flow are well known. Oscillatory barotropic forcing increases the time-averaged exchange rate (Armi and Farmer, 1986; Helfrich, 1995), but to what degree depends on the nature of the flow, the environment, and the tide.

Time-dependent exchange flow was initially studied by continually adjusting the steady case as the barotropic forcing changed. This quasi-steady approximation assumes the Froude number changes slowly enough that the flow evolves through a series of steady state regimes (Armi and Farmer, 1986; Farmer and Armi, 1986). The quasi-steady approximation is valid if the wave speeds are fast relative to the strait's dimensions, but yields exaggerated exchange flows if the wave speeds are slow (Helfrich, 1995).

In order to differentiate between exchange flows with different wave speeds and strait geometries, Helfrich (1995) introduced a non-dimensional parameter γ to the unsteady forcing problem:

$$\gamma = \frac{(g'H)^{\frac{1}{2}}T}{L} \tag{1.4}$$

where T is the tidal period, L the length of the strait, and H is the water depth at the sill peak. In the maximal case, as γ increases, exchange flow increases (Figure 1.4). Only when γ is large, thus where internal wave speeds are high and the sill is short, does the quasi-steady approximation become valid in the maximal case (Helfrich, 1995).

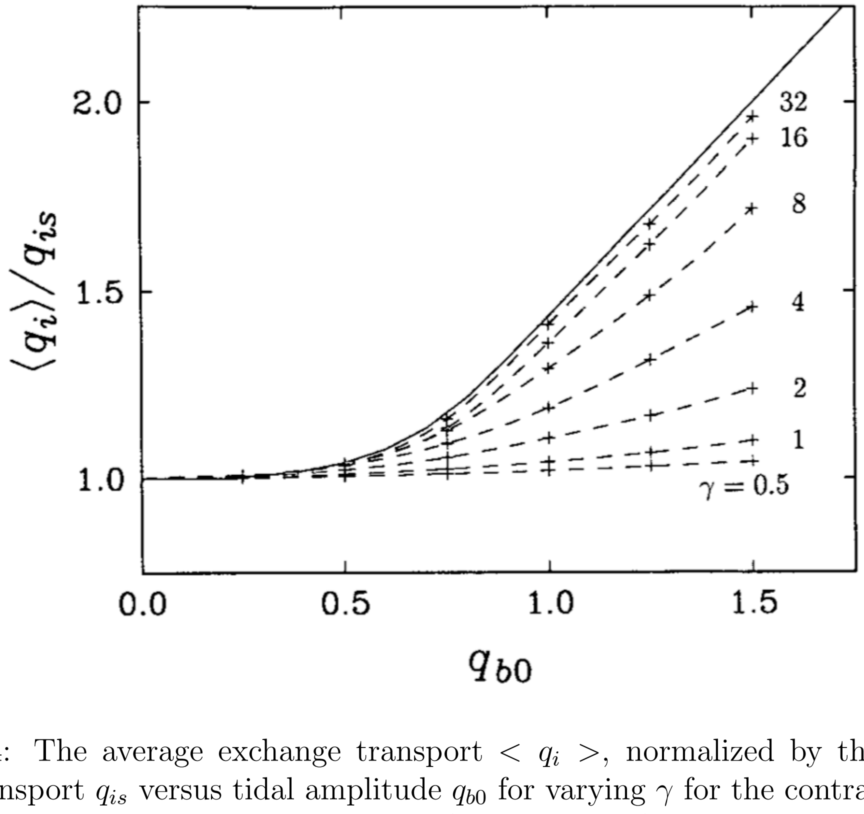

Figure 1.4: The average exchange transport $< q_i >$, normalized by the unforced steady transport q_{is} versus tidal amplitude q_{b0} for varying γ for the contraction case. The solid curve is the quasi-steady theory (Helfrich, 1995).

In the maximal case, exchange flow increases monotonically with tidal amplitude in the cases of a horizontal constriction and the combination of a constriction and sill (Helfrich, 1995). The increased exchange with tidal amplitude, when normalized by the steady-state exchange, is dependent on γ, with this rate increasing with γ until it reaches the quasi-steady approximation limit (Figure 1.4). This quasi-steady case approaches a slope of π^{-1} as q_{b0} increases.

In this study we extend Helfrich (1995), who only considered maximal exchange flows, by considering sub-maximal exchange flow under barotropic tidal forcing. We duplicate the numerical model used to study the time-dependent maximal case, and extended it to sub-maximal regimes in the sill-controlled problem in order to determine how the exchange reacts to barotropic forcing. Time-dependent sub-maximal exchange flow likely departs from steady hydraulic theory similarly to the maximal case, and how this response to barotropic forcing differs in sub-maximal flows will be determined. As many exchange flows are sub-maximal and time-dependent in nature, results will be applicable to a number of natural systems.

As we see below, three parameters define our problem: γ, as discussed above, q_{b0}, the barotropic forcing, and h_1, the unforced depth of the interface in the dense basin, and hence representing the maximality of the unforced exchange flow (Figure 1.2). We explore this parameter space and attempt to find a common way to explain the exchange flow as the flow becomes more sub-maximal. To keep things “simple” we only consider one geometry configuration, that of a Gaussian sill in a channel with no constriction.

First we review hydraulic theory used to study two-layer exchange flows in chapter two. Then we introduce our numerical model used to study time dependent barotropic forcing of the exchange flow in chapter 3. In chapter 4 we test the model against hydraulic theory and maximal time-dependent results to make sure modeled results are correct. Time-dependent sub-maximal results are shown in chapter 5, and summarized and discussed in chapter 6.

Chapter 2

Theory

Hydraulic theory developed to describe sub-maximal and maximal exchange flows in the absence of barotropic forcing will be used to verify our numerical model results. Time-independent (steady) exchange flow over a sill has been studied using steady hydraulic theory (Armi, 1986; Farmer and Armi, 1986). Hydraulic theory has relied heavily on the use of the Froude Numbers F_i^2 and G^2 presented earlier, to define the flow in terms of criticality, and map its development along the channel. In order to represent results in the Froude-Number plane, it is useful to introduce volume flux q_i,

$$q_i = u_i b y_i \tag{2.1}$$

y_i and u_i can be written in terms of Froude Numbers F_i and volume flux q_i;

$$y_i = (\frac{q_i^2}{g' b^2})^{\frac{1}{3}} F_i^{-\frac{2}{3}} \tag{2.2}$$

$$u_i = (\frac{q_i g'}{b})^{\frac{1}{3}} F_i^{\frac{2}{3}} \tag{2.3}$$

In steady flow, volume flux q_i is constant, thus the dimensionless y_i' can be found in terms of F_i. Primes from now on indicate dimensionless parameters. Here, $b' \equiv \frac{b}{b_0}$ where b_0 is the minimum strait width, and $y_i' \equiv \frac{y_i}{H}$ where H is the total depth of the sill crest;

$$y_i' = (\frac{q_i'}{b'})^{\frac{2}{3}} F_i^{-\frac{2}{3}}, \tag{2.4}$$

and the dimensionless volume flux q_i' is defined;

$$q_i' \equiv \frac{q_i}{g'^{\frac{1}{2}} b_0 (y_1 + y_2)_0^{\frac{3}{2}}}. \tag{2.5}$$

Finally, using dimensionless sill definition $h_s' \equiv \frac{h_s}{H}$, we include the rigid-lid approximation;

$$y_1' + y_2' + h_s' = 1 \tag{2.6}$$

Using equations 2.4 and 2.5, and using $q_r = \frac{q_1}{-q_2}$ as a description of the barotropic forcing present, F_1 and F_2 can be compared;

$$q_r^{\frac{2}{3}} F_1^{-\frac{2}{3}} + F_2^{-\frac{2}{3}} = \left(\frac{q_2'}{b'(1 - h_s')^{\frac{3}{2}}}\right)^{-\frac{2}{3}} \tag{2.7}$$

With no barotropic forcing, $q_r = 1$ as defined by the conservation of mass. For a given q_r, q_2', b' and h_s', a family of solutions can be found using equation 2.7 in terms of a relation between F_1 and F_2.

With a strait of constant width and a sill, the dimensional Bernoulli equations can be defined (Armi, 86);

$$H_1 = \frac{1}{2}\rho_1 u_1^2 + \rho_1 g(y_1 + y_2 + h_s) + p \tag{2.8}$$

$$H_2 = \frac{1}{2}\rho_2 u_2^2 + \rho_1 g y_1 + \rho_2 g(y_2 + h_s) + p. \tag{2.9}$$

In order to remove pressure from the problem, the equations 2.8 and 2.9 can be subtracted;

$$\frac{H_1 - H_2}{g'\rho_2 H} + 1 = y_1'(1 + \frac{1}{2}F_1^2) - \frac{1}{2}y_2' F_2^2 \tag{2.10}$$

Defining for simplicity;

$$Y_1' \equiv \frac{H_1 - H_2}{g'\rho_2 H} + 1 \tag{2.11}$$

the Bernoulli equation then becomes another relation between F_1 and F_2;

$$F_2^2 = q_r(2F_1^{-\frac{2}{3}} + F_1^{\frac{4}{3}} - 2Y_1' q_1'^{-\frac{2}{3}})^{\frac{3}{2}} \tag{2.12}$$

Equation 2.12 can now be used to relate F_1 and F_2 for any given q_r, Y_1', and q_1'. According to conservation of mass, $q_r = 1$ in the steady exchange flow problem with no barotropic forcing. The definition of hydraulic control states that $G^2 = 1$ at the sill crest, and Y_1' and q_1' are dependent upon the conditions in the deep reservoir. Subtracting equation 2.9 from equation 2.8;

$$H_1 - H_2 = \frac{1}{2}(\rho_1 u_1^2 - \rho_2 u_2^2) + g(\rho_1 - \rho_2)(y_2 + h_s) \tag{2.13}$$

We can now calculate Y_1' using 2.11 in the steady case with no barotropic forcing.

$Y_1' {q_1'}^{-\frac{2}{3}}$ is used as a definition of the exchange flow in the hydraulic theory above. Defining this parameter and putting it into equation 2.12, the theoretical progression of the flow along the strait in the Froude number plane (F_2^2 vs. F_1^2) can then be found.

The results of the numerical model presented in chapter 3, can show the progression of the flow along the strait in the Froude number plane. For example, the model was used to create figure 1.2, where three steady flows are displayed in the Froude number plane, as calculated from the modeled results. The parameter $Y_1' {q_1'}^{-\frac{2}{3}}$ is also calculated from the modeled results using equations 2.11 and 2.13 at the sill crest, and in figure 1.2 results indicate that $Y_1' {q_1'}^{-\frac{2}{3}} = 1.4762$ (Top), $Y_1' {q_1'}^{-\frac{2}{3}} = 2.5593$ (Middle), and $Y_1' {q_1'}^{-\frac{2}{3}} = 14.8374$ (Bottom). Putting these values into equation 2.12 reveals the theoretical progressions of the flows in the Froude number plane. These theoretical flow progressions can then be compared to the modeled result. If these flow progressions are equal, the modeled result is theoretically consistent. This technique is used in chapter 4 in order to test the accuracy of the model.

Chapter 3

Numerical Methods

We now explain the model used to study time-dependent exchange flows, duplicated from Helfrich (1995). This model extends hydraulic theory to include time-dependent barotropic forcing to predict these inherently non-linear flows. Helfrich used this technique to study maximal exchange flows, and we extend it to include sub-maximal flows.

Some simplifying assumptions were made (Helfrich, 1995). First, the flow was assumed to be hydrostatic. Hydrostatic models assume an exact balance between pressure and density fields, in turn gravity. This is justified by the typical geophysical scale of these flows, and is congruent with the theoretical treatment of steady flows. The hydrostatic approximation can limit the applicability of hydraulic theory. The terms omitted from the momentum equations due to this simplification are often thought to be small on large scale flows, and thus any small-scale hydrostatic phenomena are ignored (Manning et al., 2010). The hydrostatic approximation also affects rotation in the model by neglecting the horizontal coriolis term (Marshall et al., 1997). Some exchange flows occur in areas wider than the internal Rossby number, where the coriolis force can have a distinct effect on the exchange flow (Valle-Levinson, 2008). In these cases, the horizontal density gradient across the width of the straight could be large, and this simplification would not be accurate.

Second, the exchange was simplified to include two density layers. Multiple intermediate density layers can be added either analytically or numerically (Baines, 1995), and the existence of these layers have been found to play an important role in exchange flow (Winters and Seim, 2000), but we do not add this complexity here.

Third, the effects of viscosity and mixing between the layers is not included. The addition of interfacial friction to the problem has been found to result in hydraulic controls similar to those modeled in the inviscid case (Gregg and Özsoy, 2002). Interlayer transport due to entraiment and mixing between layers is known to case a deviation of simulated maximal exchange flow from predicted flows, causing lower Froude numbers, larger transports, and wider subcritical regions along the strait (Winters and Seim, 2000). Both density layers lose fluid to interfacial layers, which then carries a significant fraction of horizontal transport. This entrainment is greatest from the fastest layer, as well as downstream, where dense layer velocity is maximized. Bottom friction, which is likewise neglected here, has been found to alter the dynamics of exchange flows, shifting them towards the sub-maximal (Winters and Seim, 2000). Bottom stresses can act to inhibit the development of supercritical flow, thus fighting the existence of maximal flow (Winters and Seim, 2000).

We use Helfrich's (1995) numerical model depicting the time-dependent maximal exchange flow problem. A numerical model was used because hydraulic quasi-steady physical theory was found to only apply to a subset of maximal exchange flows defined by γ, thus it is likely that this theory does not accurately describe the non-linearity of many time-dependent sub-maximal flows. This model takes the physical form of a strait separating infinitely large basins (Figure 1.4), and simulates the effect that variable tidal forcing and strait geometry have on maximal exchange flow. Control over the flow was established by either a horizontal constriction, a sill, or a combination of the two, simplifying the momentum equations as follows.

The momentum equations below utilize the following normalizations: u_i is normalized by $(g'H)^{\frac{1}{2}}$ where $g' = g\frac{\rho_2-\rho_1}{\rho_2}$, x, the distance from the center of the strait centered at zero, and y_i, the thickness of the i^{th} layer, are normalized by H, t by $(\frac{H}{g'})^{\frac{1}{2}}$, and a_i, the cross-sectional area of each layer, is normalized by $A_0 = b_0H$.

$$\frac{\partial u_i}{\partial t} + \frac{\partial}{\partial x}[\frac{u_i^2}{2} + (1-i)y_1 + \frac{1}{\sigma}(y_1 + y_2 - h_s)] = 0 \tag{3.1}$$

Here $h_s(x)$ is the depth of the strait at the sill crest (Figure 1.3).

The continuity equation takes the form

$$\frac{\partial a_i}{\partial t} + \frac{\partial}{\partial x}(a_i u_i) = 0 \tag{3.2}$$

where a_i represents the along-strait area of each layer;

$$a_i = b(x)y_i \tag{3.3}$$

Here $b(x)$ is the variable width of the strait, and must be defined.

The density difference between layers is assumed to be small compared to water's density, $\sigma << 1$, allowing the Boussinesque and rigid-lid approximations to be used:

$$y_1 + y_2 = 1 + h_s \tag{3.4}$$

The barotropic transport q_b becomes a function of time but not space;

$$q_b(t) = u_1 a_1 + u_2 a_2 \tag{3.5}$$

Equations 3.1 and 3.2 can now be simplified to contain only two unknown quantities; a_1 and shear $U = u_2 - u_1$:

$$\frac{\partial a_1}{\partial t} + \frac{\partial}{\partial x}[\frac{a_1 q_b + U a_1^2}{A} - U a_1] = 0 \tag{3.6}$$

$$\frac{\partial U}{\partial t} + \frac{\partial}{\partial x}[\frac{U q_b + U^2 a_1}{A} - \frac{a_1}{b} - \frac{U^2}{2}] = 0 \tag{3.7}$$

Here, $A(x)$ represents the total area of the strait:

$$A(x) = a_1 + a_2 = b(1 + h_s) \tag{3.8}$$

The imposed barotropic tide is defined;

$$q_b(t) = q_{b0} sin(2\pi \frac{t}{T}) \tag{3.9}$$

where

$$q_{b0} = \frac{u_{b0}}{(g'H)^{\frac{1}{2}}} \tag{3.10}$$

Here, u_{b0} represents the dimensional velocity of the barotropic forcing where $A = 1$. Finally, variables x and t are rescaled;

$$\tau = \frac{t}{T} \tag{3.11}$$

where T is the tidal period, and

$$\zeta = \frac{x}{L} \tag{3.12}$$

where L is a length scale of the strait.

Equations 3.6 and 3.7 then become;

$$\frac{\partial a_1}{\partial \tau} + \gamma \frac{\partial}{\partial \zeta}(\frac{a_1 q_b(\tau) - U a_1 A + U a_1^2}{A}) = 0 \tag{3.13}$$

and

$$\frac{\partial U}{\partial \tau} + \gamma \frac{\partial}{\partial \zeta}(\frac{U q_b(\tau) + U^2 a_1}{A} - \frac{a_1}{b} - \frac{U^2}{2}) = 0 \tag{3.14}$$

The solutions to the system of equations 3.9, 3.13, and 3.14 then depend on only two non-dimensional parameters, q_{b0} and γ:

$$\gamma = \frac{(g'H)^{\frac{1}{2}} T}{L} \tag{3.15}$$

In the case of a strait with no sill, the horizontal constriction was defined as

$$b(\zeta) = 1 + 4(1 - e^{-\alpha^2 \zeta^2}) \tag{3.16}$$

Sills were defined by the equation

$$h_s(\zeta) = 1 - sech^2(\beta\zeta) \tag{3.17}$$

The sill-constriction combination can include a constriction laterally offset from that of the sill crest:

$$b(\zeta) = \frac{1}{2} + \frac{3}{2}(1 - e^{-\alpha^2(\zeta-1)^2}) \tag{3.18}$$

The channel width is tested away from the contractions, and are made very large to simulate large reservoirs not affected by the exchange flow for the duration of the runs made here. The sill ends at $\zeta = \pm 1$, and strait width b was increased from $\zeta = 8$ to $\zeta = 16$, the end of the domain length. In this area, b was increased linearly from $b = 1$ to $b = 100$. Comparing the results between this strait and one holding $b = 1$ for the length of the strait, there is no observable difference between exchange flow results at the sill, thus this definition can be relaxed. The results discussed in this paper were found after relaxing this definition, and thus in a long strait of constant area.

Equations 3.13 and 3.14 were solved using the Two-Step Lax-Wendroff scheme (Press et al., 1988). In order to apply this scheme, the two unknown variables a_1, and U were combined into vector $\mathbf{M}$, where $M_1 = a_1$ and $M_2 = U$. Next, fluxes Fl_1

and Fl_2 are introduced such that

$$Fl_1 = \gamma(\frac{a_1 q_b(\tau) - U a_1 A + U a_1^2}{A}) \tag{3.19}$$

and

$$Fl_2 = \gamma(\frac{U q_b(\tau) + U^2 a_1}{A} - \frac{a_1}{b} - \frac{U^2}{2}) \tag{3.20}$$

With these definitions in place, equations 3.13 and 3.14 can now be written as one system;

$$\frac{\partial}{\partial\tau}\mathbf{M} = -\frac{\partial}{\partial\zeta}\mathbf{Fl(M)} \tag{3.21}$$

Intermediate values $M_{j+1/2}^{n+1/2}$ (where M_j^n denotes $M(x_j, t_n)$) were defined;

$$\mathbf{M}_{j+1/2}^{n+1/2} = \frac{1}{2}(\mathbf{M}_{j+1}^n + \mathbf{M}_j^n) - \frac{\Delta\tau}{2\Delta\zeta}(\mathbf{Fl}_{j+1}^n - \mathbf{Fl}_j^n) \tag{3.22}$$

$\mathbf{M}_{j+1/2}^{n+1/2}$ were used in equations 3.19 and 3.20 to calculate intermediate fluxes $\mathbf{Fl}_{j+1/2}^{n+1/2}$, which could be used to determine $\mathbf{M}_j^{n+1}$ using the equation;

$$\mathbf{M}_j^{n+1} = \mathbf{M}_j^n - \frac{\Delta\tau}{\Delta\zeta}(\mathbf{Fl}_{j+1/2}^{n+1/2} - \mathbf{Fl}_{j-1/2}^{n+1/2}) \tag{3.23}$$

This process could then be repeated for all steps in ζ and τ.

The Sommerfeld radiation boundary was used on both ends of the strait (Helfrich, 1995):

$$\phi_\tau - c\phi_\zeta = 0 \tag{3.24}$$

where $\phi = a_i$ and U, and c is the phase velocity near the boundaries. This boundary condition describes an open boundary, shown to be free of reflection for single wave propagation (Orlanski, 1976). The domain length is telescoped away from the sill to ensure that if reflections do exist, they do not reach the sill in time to affect results. Flow left of the sill is defined through the model and initial conditions to be supercritical, which helps information exit the domain. Boundary conditions allow the flushing of either layer from the sill region for large barotropic forcing.

Initially, the model was run as a lock-exchange problem, and allowed to reach a relative steady state, which represented the maximal case. M_1 and M_2 along the straight in this steady case was then used as the initial condition for all maximal exchange cases. The initial conditions for sub-maximal flows were similarly found, using a lock exchange problem, but varying h_1 initially. The initial conditions were derived from the model itself, and are stable within its parameters. In the next chapter we test that these results are valid.

In order to dampen growth of instabilities that occur in the model, a dissipation term $\nu U_{\zeta\zeta}$ where ν is a constant, is added to the right hand side of equation 3.14 (Helfrich, 1995). This dissipation acts to model small-scale mixing that may occur in real exchange flows. Without dissipation, numerical instabilities arise, especially as q_{b0} is increased, which grow uncontrollably and affect the solution. In addition to damping high wave-number instabilities, this term also reduces numerical oscillations that occur due to shock disturbances. As tidal amplitude increases, so too does the size of the shocks emitted downstream. The advection scheme being used does a poor job of preserving shocks, thus viscosity needed to be added.

The dissipation term was tested to ensure that it reduced instabilities without affecting average exchange calculated at the sill crest. Most disturbances were observed to occur in the light basin, where shocks and internal waves develop and travel. The damping term was thus added only to the left of the sill ($\zeta < -1$, Figure 1.2), leaving the immediate sill area and the strait to the right untouched by dissipation effects. Applying dissipation only left of the sill helped to ensure that dissipation effects did not affect the exchange flow at the sill crest.

Chapter 4

Testing the Numerical Model

Here we test the numerical model against known and previous solutions to ensure that the numerics are up to the task of simulating these flows. Three tests are performed - the first is steady maximal exchange flow between two basins for which the solution can be derived analytically, and was simulated by Helfrich (1995). Second, we reproduce the barotropically forced maximal exchange flows presented by Helfrich (1995). Third, we test that the model can simulate sub-maximal steady exchange based on the results presented in Farmer and Armi (1986).

4.1 Steady Test - No Barotropic Forcing

In order to test the accuracy of the model in comparison to Helfrich (1995), steady maximal flow results in the absence of barotropic forcing are duplicated. Helfrich modeled two-layer exchange in a strait under these conditions, with a sill and offset horizontal constriction as topographic controls. The light water reservoir lies left of the sill, and the dense reservoir to the right. The light fluid is traveling left to right as the dense water travels right to left under the action of gravitational forcing. The sill is defined by equation 3.17, with the sill crest at $\zeta = 0$ where $b = 1$. The narrows is defined by equation 3.18. Here, $\beta = 3.75$, $\alpha = 0.637$ for $\zeta \leq 1$, and $\alpha = 1.273$ for $\zeta \geq 1$.

For our results, the steady transport with no barotropic forcing is $q_{is} = 0.137$, agreeing with Helfrich (1995). The interface between density layers, the composite Froude number G, and the value $\frac{U^2}{y_1+y_2}$ are also duplicated (Figure 4.1).

This example is instructive to help describe exchange flows. As previously stated,

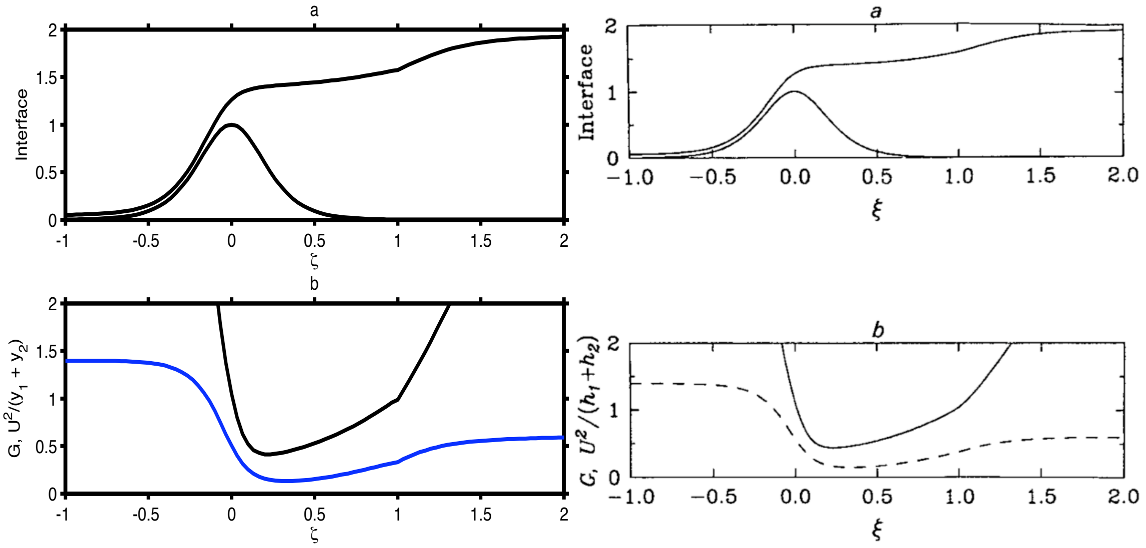

Figure 4.1: Results using our code (left) duplicate past results (right, Helfrich 1995) in the sill-constriction combination case. Figures 'a' display the interface along the strait between density layers, and figures 'b' display Froude number G and value $\frac{U^2}{y_1+y_2}$. Steady Maximal Exchange case in sill-narrows combination case (Helfrich, 1995). The lateral constriction is centered at $\zeta = 1$. Flow is critical at the constrictions $\zeta = 0, 1$, with sub-critical flow between, and super-critical flow in the reservoirs.

maximal exchange occurs when the dense reservoir has the internal interface close to the surface. The composite Froude number G^2 describes the criticality along the channel (Figure 4.1, lower panels, solid black). We can see that the flow is critical, and thus $G^2 = 1$, at the two controls at $\zeta = 0$ and $\zeta = 1$ Flow is sub-critical between the two controls. Outside of this control area, flow is supercritical as $G > 1$; in these areas, we can see one layer becomes comparatively thin, resulting in supercritical flow. Left of the sill, the dense layer flows down the sill and accelerates and right of the constriction the light layer accelerates along the surface towards the dense reservoir.

The parameter $\frac{U^2}{y_1+y_2}$ (Figure 4.1, lower panels, blue or dashed) describes the difference in layer speeds along the channel as $U = u_2 - u_1$. Left of the sill crest, where dense water flows down the sill supercritically, and the light layer is strong and comparatively slow, $\frac{U^2}{y_1+y_2} > 1$. Elsewhere the light layer travels faster than the dense layer, and $\frac{U^2}{y_1+y_2} < 1$, where the light layer is traveling more quickly than the dense layer below.

4.2 Time-Dependent Results

Having duplicated the exchange flow in the absence of barotropic forcing, the time-dependent problem in a simple strait whose control is a horizontal constriction defined by equation 3.16 is now re-created. Helfrich (1995) displayed the progression of the time-averaged exchange flow $< q_i >$ as a function of tidal amplitude q_{b0}. It is convenient to normalize by the steady state exchange q_{is}, the exchange flow in the absence of barotropic forcing. The ratio $\frac{<q_i>}{q_{is}}$ was found to increase monotonically with q_{b0} at each γ. Similarly, $\frac{<q_i>}{q_{is}}$ increased with γ at a given q_{b0}, tending towards the quasi-steady theory as $\gamma > 30$.

Our numerics replicate these results (Figure 4.2). The results between models are not compared exactly, as different γ values are used. However, in both cases $(\frac{<q_i>}{q_{is}})$ increases monotonically with both q_{b0} and γ. In the new model, the curve representing $\gamma = 1.8$ progresses to approximately $\frac{<q_i>}{q_{is}} = 1.25$ near $q_{b0} = 1.5$, similar to the $\gamma = 2$ curve displayed by Helfrich (1995). As γ becomes large, the curves separating cases at high tidal amplitude do not vary as wildly with γ. Additionally, at these high-γ cases, exchange approaches $(\frac{<q_i>}{q_{is}} = 2)$ as tidal amplitude approaches $q_{b0} = 1.5$. This test shows that the time-dependent maximal exchange flow is adequately represented by the current numerics, and can be applied to the sub-maximal case with confidence.

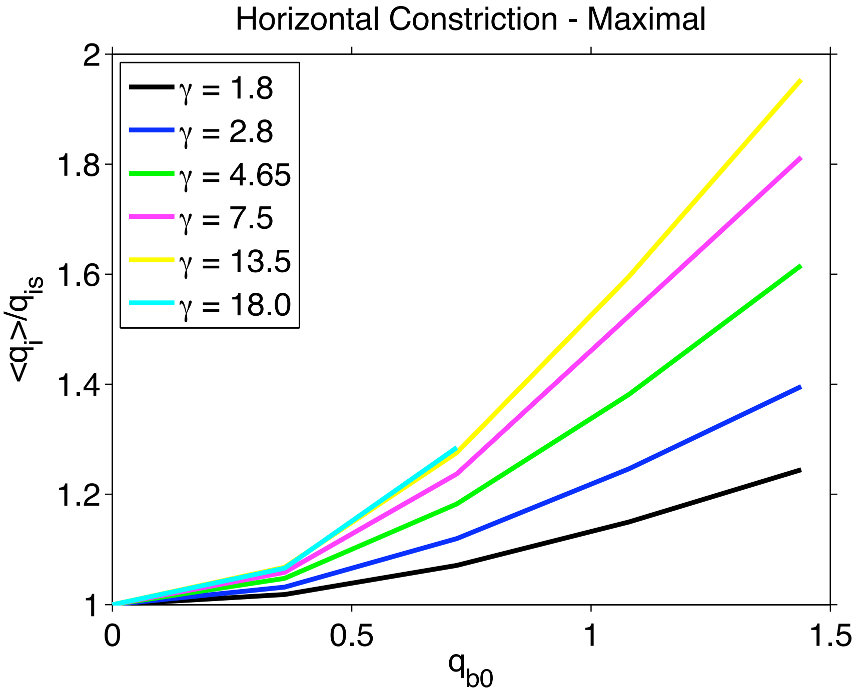

Figure 4.2: Time-averaged exchange flow $< q_i >$ normalized by the steady state exchange q_{is} as a function of tidal amplitude q_{b0} for different values of γ in the horizontal constriction case. These results are duplicate Helfrich's (1995, compare to our Figure 1.4, above)

4.3 Sub-Maximal Flow and Hydraulic Theory

Our numerics can replicate the results in Helfrich (1995), but as a final test, we compare to steady sub-maximal hydraulic theory. For an exchange flow problem in a channel with a sill, equations 2.7 and 2.12 are used to relate F_1^2 to F_2^2 depending on $\frac{q_2'}{b'(1-h_s')^{\frac{3}{2}}}$ and $Y_1'q_1'$. Solution curves can be represented in the Froude number plane for all theoretical steady state exchange flows (Figure 4.3). $q_1 = -q_2$ in this steady case due to conservation of mass, therefore $q_r = 1$. At the sill $F_1^2 + F_2^2 = 1$, and both F_1^2 and F_2^2 tend to zero away from the sill in an infinite reservoir.

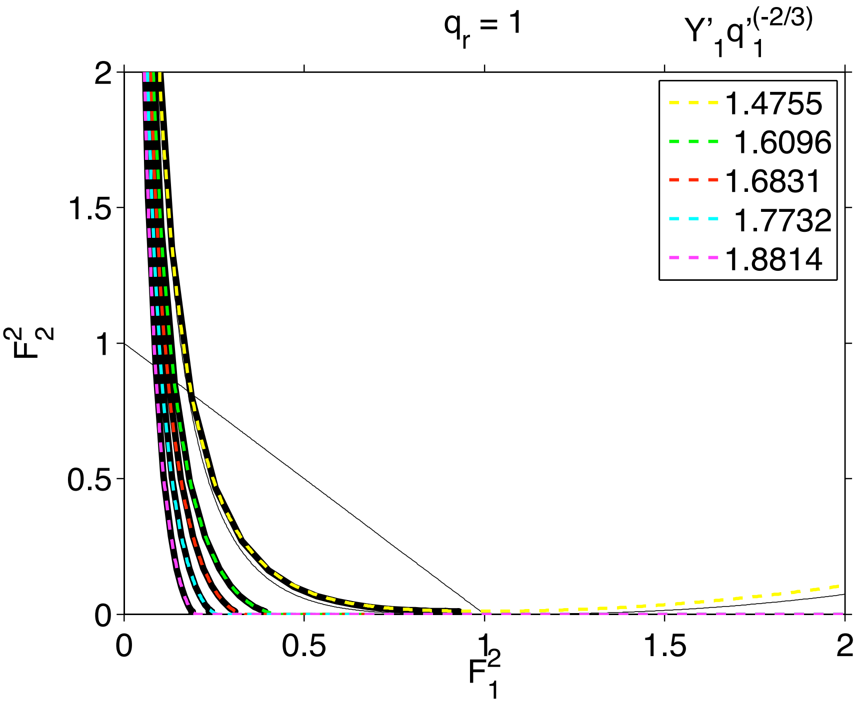

Figure 4.3: Comparison of hydraulic theory (colored lines) and the numerical solutions (black lines), a pair of curves for unique values of $Y_1'q_1'^{(-2/3)}$ found from model results. The thin curve represents the theoretical maximal solution (Farmer and Armi, 1986).

In a strait of uniform breadth containing a sill, one solution curve from each of equations 2.7 and 2.12 were found to represent maximal exchange. For equation 2.7, this was $q_2' = 0.208$, and for equation 2.12, $Y_1'q_1'^{\frac{-2}{3}} = 1.5$ (Farmer and Armi, 1986). The modeled results are similar to the theory (Figure 4.3) with $q_2' = 0.211$ and $Y_1'q_1'^{\frac{-2}{3}} = 1.4755$. According to these results, the model closely reflects the expected results in this maximal case.

In order to verify model results in the steady sub-maximal case using hydraulic theory, the model is run with five interface heights in the dense reservoir, one maximal and four sub-maximal. The curves of Froude numbers F_2^2 versus F_1^2 along the strait are plotted from the results (Figure 4.3). The term $Y_1'q_1'^{(-2/3)}$, a term similar to h_1 and relating to the initial conditions, is calculated from the results of each run using the process explained previously in chapter 2. This term is then used in equation 2.12, and using $q_r = 1$, the theoretical curve relating to these calculated values is plotted for each run (colored dashed lines). The theoretical results and the modeled results are equal, showing that in the solely sill-controlled steady case, the model agrees with hydraulic theory.

Figure 4.3 displays the development of criticality as the flow regime deviates from maximal to sub-maximal flow. The thin line in this figure represents criticality ($G^2 = 1$), supercritical flow exists above this line ($G^2 > 1$), and subcritical flow below ($G^2 < 1$).

In each case, flow left of the sill crest is represented by the supercritical area of the curve. The dense layer, represented here by F_2^2, flows down the sill towards the light reservoir (Figure 1.2). Right of the sill, critical and supercritical flow can only exist in the maximal case. Thus in straits lacking a second control, the maximal case represents the steady state flow where the light layer approaches the wave velocity of the channel downstream. The light layer maximum velocity is lower in sub-maximal flows, and never approaches the wavespeed in the strait, remaining sub-critical right of the sill.

We have successfully tested our numerics against past hydraulic theory in the sub-maximal and maximal cases. Similarly, maximal steady and time-dependent model results with differing strait definitions have been successfully duplicated. Having passed these tests, the present numerical model is now extended to study the sub-maximal time-dependent case.

Chapter 5

Exchange in Sub-maximal Tidally Forced Flows

Here we extend the results from Helfrich (1995) to explore the exchange flow over a sill under barotropic (tidal) forcing. First we check that the parameter $\gamma = \frac{(g'H)^{\frac{1}{2}}T}{L}$ adequately non-dimensionalizes the sill-only problem we are interested in here. Second, we test the quasi-steady nature of the flow as a function of γ. If the flow were quasi-steady, we could simply use steady-state theory to predict the exchange, however we see below that this is a poor approximation except for the cases with very high γ. Finally, we study the main goal of this work, which is quantifying the enhanced exchange over the sill in the presence of barotropic tidal forcing.

5.1 Applicability of γ

As discussed previously, maximal exchange flow normalized by the steady-state exchange ($\frac{<q_i>}{q_{is}}$) has been found to increase monotonically with tidal amplitude q_{b0} at a rate that depends on $\gamma = \frac{(g'H)^{\frac{1}{2}}T}{L}$ (Helfrich, 1995). Exchange flows in straits with higher γ experience a greater increase in tidally averaged exchange when normalized by the steady state exchange q_{is} than exchange flows in straits with smaller γ.

We test the applicability of dimensionless parameter γ. If results are constant with γ held constant regardless of changes in g' or L, exchange flows of different sills can be related, and the dimensions of the parameter space to be explored are reduced. For this study, L is defined as the gaussian half-width of the sill in the absence of a horizontal constriction, whereas for the sill-contraction combination, L

was the distance between the sill and narrows (Helfrich, 1995).

Five cases of reduced gravity g' were studied with differing definitions of L and g', all with $\gamma = 21.844$. The examples range in reduced gravity g' as follows: $g' = 86.9$, 311.1, 805.81, 1601.5, and 2746.3. The time-averaged increase in exchange flow with q_{b0} in all cases are equal (Figure 5.1), showing that γ is a useful way to relate exchange flows with differing sill geometry. This is a new result, showing that sill length is an important factor in affecting time-dependent exchange flow. Results relating to parameter γ in the combined sill-horizontal constriction case illustrate that results varied slightly with geometric changes of the strait even if γ was kept constant (Helfrich, 1995). The distinction between the definition of L is likely the cause of this difference, in which Helfrich's distance between the crest and constriction may have had an effect from the half-width of the sill as well that the single L parameter did not account for.

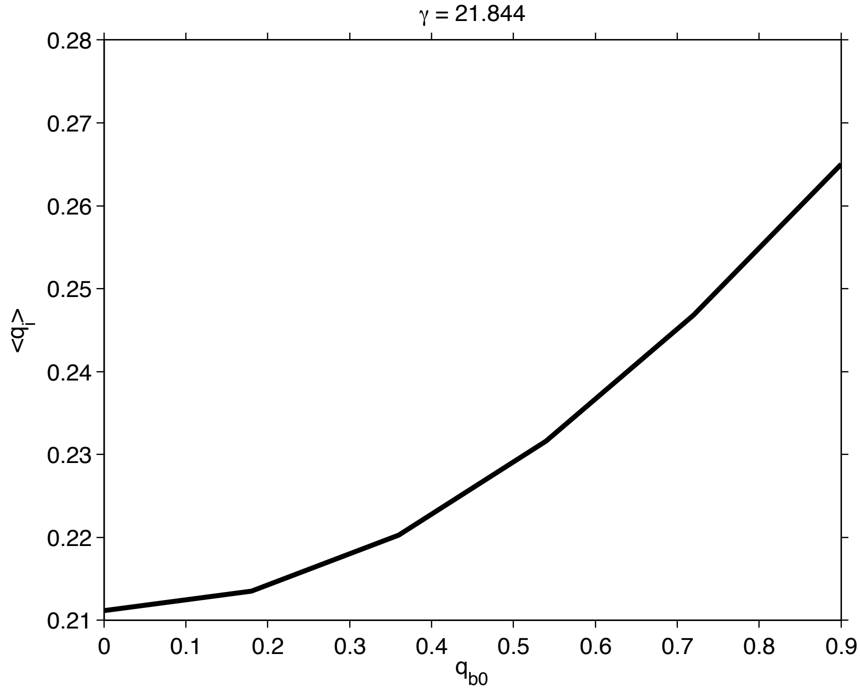

Figure 5.1: Time-averaged dimensional exchange $< q_i >$ against tidal amplitude q_{b0} at $\gamma = 21.844$. L and g' have been varied 5 times, all keeping γ constant, all giving the same results displayed above. Values of g' used are $g' = 86.9$, 311.1, 805.81, 1601.5, and 2746.3.

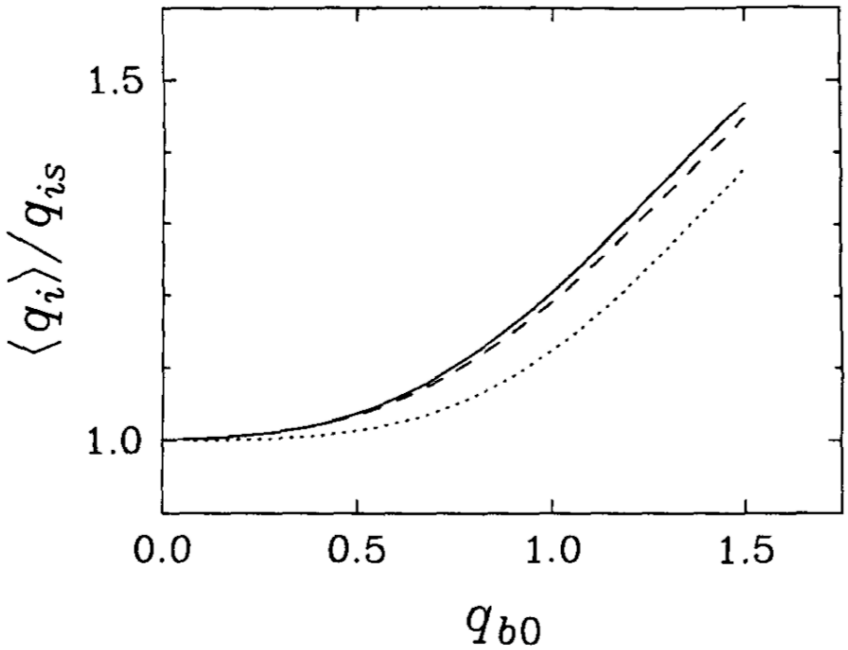

Figure 5.2: Past results comparing normalized average transport for three straits of constant $\gamma = 4$, but varied horizontal constriction shape (Helfrich, 1995). The variation in results showed that physical attributes of the strait were needed to be taken into account to accurately predict the time-averaged exchange flow.

5.2 Is the Flow Quasi-Steady?

Acquiring a fundamental understanding of what exchange flows are quasi-steady in nature is another goal of this study. It was determined in the maximal case that for $\gamma \gtrsim 30$ time-dependent exchange flow can be approximated as quasi-steady (Helfrich, 1995). For lower γ, the system deviates from the quasi-steady case. A quasi-steady system is a time-dependent system that can be approximated as a series of steady exchange flows of different strengths. In order to make this approximation, changed forcing on the flow must result in a fast reaction of the exchange to a new near-steady state.

It is understood that as γ decreases, maximal exchange flow deviates from quasi-steady (Helfrich, 1995). The difference between these cases at constant tidal amplitude is studied through the progressions of dense layer thickness y_2 and transport q_2 at the sill (Figure 5.3). Here, the blue line represents the high-$\gamma = 31$ case, and green represents the low-$\gamma = 9.6$ case. We can see that at lower-γ, y_2 does not react as quickly to imposed forcing than the high-γ system, and doesn't reach as high or low of peaks in a tidal cycle. Similarly, q_2 is not as strong on average in the low-γ case. These results show that in the maximal case, exchange flows differ a large amount with variations in γ. This suggests that not all flows can be represented by the quasi-steady result.

The difference between high and low-γ flows in a sub-maximal case ($h_1 = 0.5593$) is also studied with similar results to the maximal case above (Figure 5.3). Again, results differ with γ, suggesting that not all exchange flows can be quasi-steady in nature.

The response of the exchange flow to step changes in the barotropic forcing at different values of γ indicates the reason for different responses at different γ. An initially steady exchange flow with no barotropic forcing is hit with strong barotropic forcing of $q_{b0} = 0.72$. The progression of transport q_2 is displayed for a maximal (Figure 5.5) and a sub-maximal exchange flow (Figure 5.6). $q_2 - q_{2eq}$, where q_{2eq} represents the equilibrium transport at $q_{b0} = 0.72$, is also displayed in each case. Any deviation of $q_2 - q_{2eq}$ from zero represents a deviation of the perfectly quasi-steady case. Both maximal and sub-maximal exchange flows deviate from the quasi-steady case. Each forcing step results in an instantaneous change to q_2, but the following adjustment to equilibrium is sizable compared to the initial step. This adjustment, even at high-γ, takes longer than a tidal period, thus is far from instantaneous. If

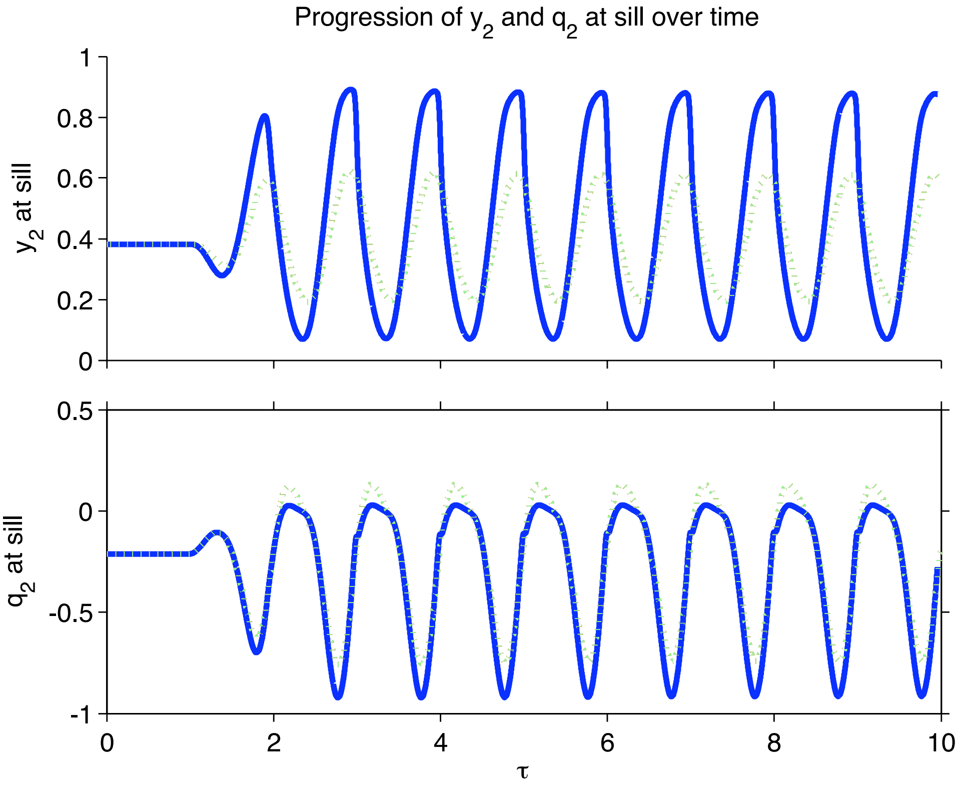

Figure 5.3: Progression of y_2 and q_2 at the sill over time at two γ cases in the maximal exchange regime defined by $h_1 = 0.3694$. Blue represents the high-$\gamma = 31$ case, and green represents the low-$\gamma = 9.6$ case. $q_{b0} = 1.08$ in all cases.

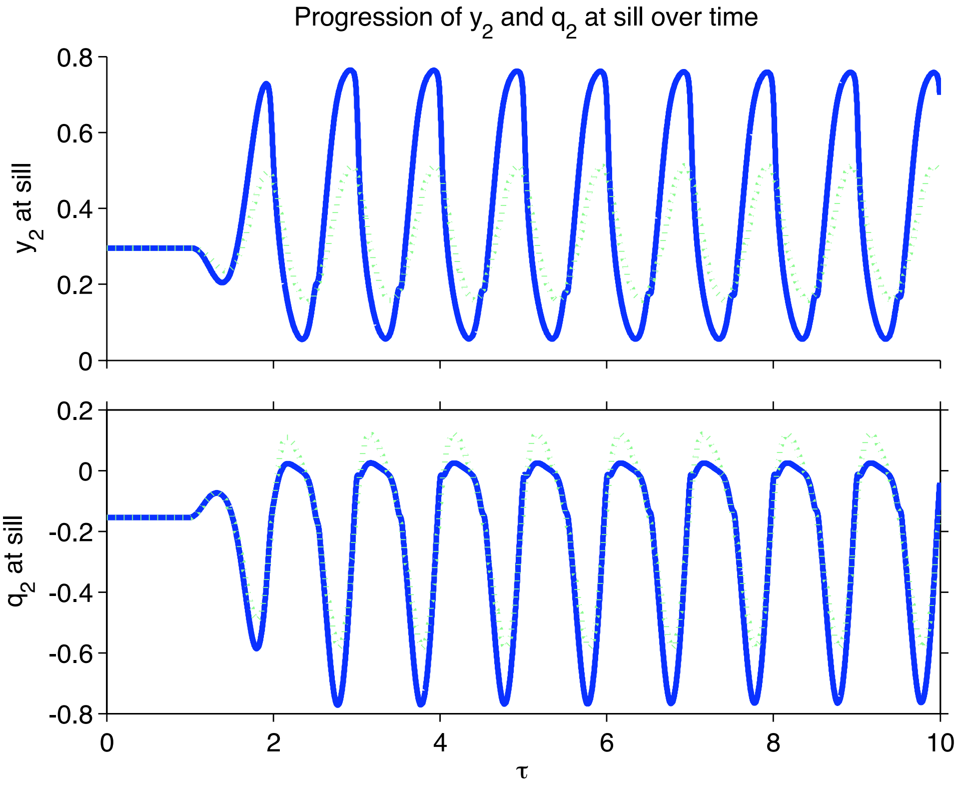

Figure 5.4: Progression of y_2 and q_2 at the sill over time at two γ cases in the sub-maximal exchange regime defined by $h_1 = 0.5593$. Blue represents the high-$\gamma = 31$ case, and green represents the low-$\gamma = 9.6$ case. $q_{b0} = 1.08$ in all cases.

the following adjustment were negligible this would would be moot, but due to the amplitude of this adjustment it is unlikely that the maximal or sub-maximal system is quasi-steady in these examples.

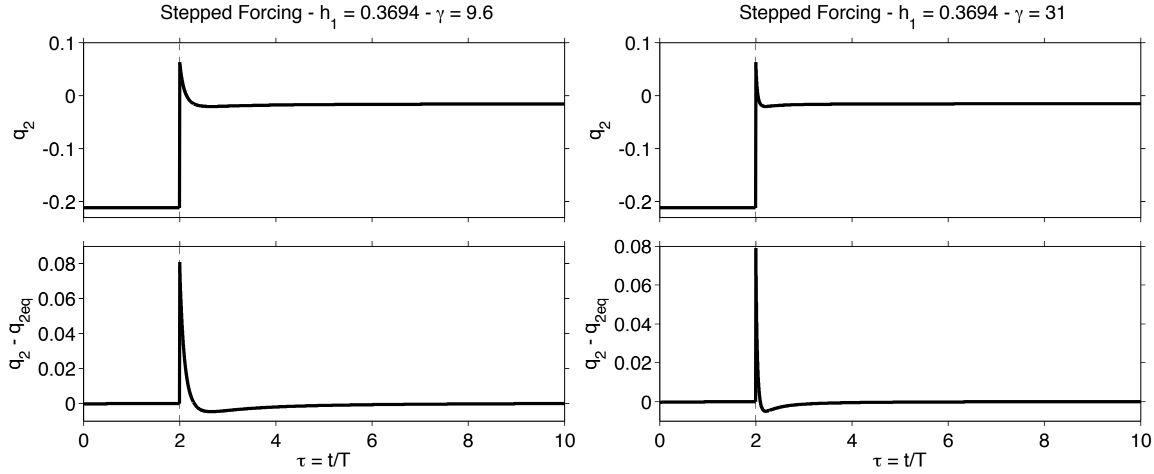

Figure 5.5: The reaction of the maximal system to increased barotropic forcing at lower γ (Left), and higher γ (Right), as seen in the development in q_2 with time. Dashed lines represent adjusted forcing, at an interval of $q_{b0} = 0.72$. $q_2 - q_{2eq}$, where q_{2eq} represents the equilibrium transport at $q_{b0} = 0.72$, is also displayed in each case (Bottom). Deviations from zero here represent deviations from quasi-steady flow.

The same test is completed at extremely high-$\gamma = 65$ (Figure 5.7). Again, the system deviates from quasi-steady, but the adjustment time to near-steady state is much quicker than in the other cases discussed above.

At lower γ ($\gamma = 9.6$), q_2 reacts immediately after each step of imposed forcing then continues to adjust to equilibrium. The time taken for q_2 to adjust to within 5% in these flows are 3.56 tidal periods in the maximal case, and 5.15 tidal periods in the sub-maximal case. When $\gamma = 31$, q_2 adjusts to within 5% of equilibrium in 1.49 and 1.63 tidal periods in the maximal and sub-maximal flows respectively. As γ increases, the time needed for q_i to reach equilibrium decreases. As this adjustment time decreases, the system relates more to the quasi-steady. It is possible that at higher γ, the adjustment time would be negligible and the system would resemble quasi-steady flow as we see in the very high-$\gamma = 62$ maximal case. However, q_2 adjusts to within 5% of equilibrium in 0.79 tidal periods in this flow.

Tidal forcing adjusts more gradually, increasing in much smaller steps than are tested here. The adjustment time needed to reach equilibrium may still apply in the

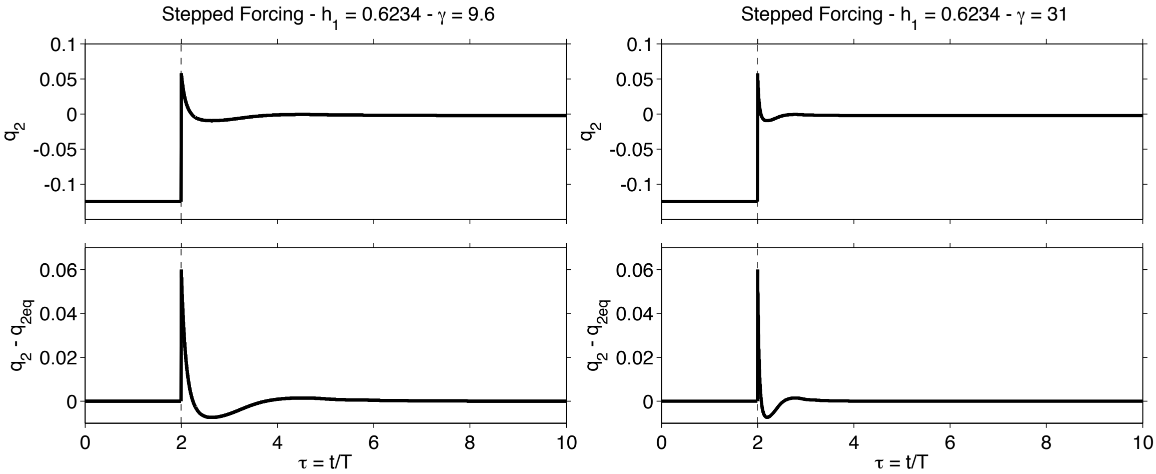

Figure 5.6: The reaction of the sub-maximal system to increased barotropic forcing at lower γ (Left), and higher γ (Right), as seen in the development in q_2 with time. Dashed lines represent adjusted forcing, at an interval of $q_{b0} = 0.72$. $q_2 - q_{2eq}$, where q_{2eq} represents the equilibrium transport at $q_{b0} = 0.72$, is also displayed in each case (Bottom). Deviations from zero here represent deviations from quasi-steady flow.

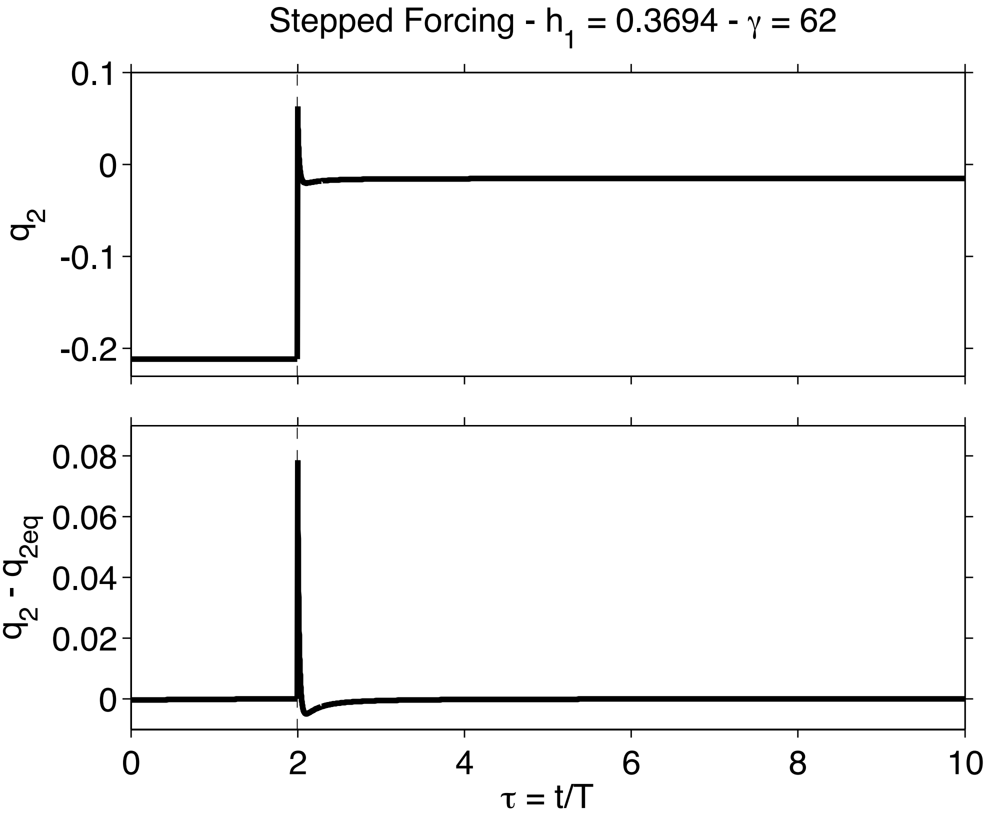

Figure 5.7: The reaction of the maximal system to increased barotropic forcing at very high-$\gamma = 62$, as seen in the development in q_2 with time. Dashed lines represent adjusted forcing, at an interval of $q_{b0} = 0.72$. $q_2 - q_{2eq}$, where q_{2eq} represents the equilibrium transport at $q_{b0} = 0.72$, is also displayed in each case (Bottom). Deviations from zero here represent deviations from quasi-steady flow.

realistic case, but the amplitude of the adjustment may vary.

5.3 Sub-maximal Exchange under Time-Dependent Barotropic Tidal Forcing

5.3.1 Phenomenology

Here we focus on quantifying the mean exchange over the sill under time-dependent barotropic forcing on exchange flows that would be Sub-maximal in the absence of the forcing. First, it is useful to consider the development of the interface between density layers, the composite Froude number G^2, and the dense layer transport q_2 throughout a tidal cycle (Figure 5.8). These variables are plotted against distance along the channel ζ at four points in the tidal cycle: leftward barotropic forcing which we will call “flood tide”, slack (“high tide”), rightward barotropic forcing (“ebb tide”), and slack again (“low tide”), as indicated by arrows.

The maximal case studied by Helfrich (1995) is represented in each plot by the solid blue line, and two sub-maximal flows are included. We first describe the maximal case, and then how the sub-maximal cases differ. The developments of composite Froude number G^2, the inter-layer interface, and dense layer transport q_2 along the strait at four points in the tidal cycle are displayed.

Maximal exchange flow in the high-γ ($\gamma = 31$), and low tidal amplitude ($q_{b0} = 0.36$) case is first examined (Figure 5.8 - Top). Similarly to the steady cases with no barotropic forcing, the G^2 plots show that flow is supercritical left of the sill. At flood tide, represented by the left-pointing arrow, flow right of the sill is sub-critical. Barotropic forcing slows the light water layer below criticality. Between flood and ebb tides, flow transitions from critical at the sill crest, to subcritical for a period right of the crest before approaching criticality. This flow is similar to that observed in the steady case with no barotropic forcing described in the Froude-Number plane (Figure 1.2). During ebb tide, represented by the right-pointing arrow, flow right of the sill crest is supercritical, as the tide accelerates the natural flow of the light layer. Again, between the tidal extremes of the ebb and flood, flow approaches criticality right of the sill after a period of subcritical flow.

The interface at the sill varies with barotropic forcing, and creates internal waves that are emitted into the dense basin. During flood tide, the interface is increasing

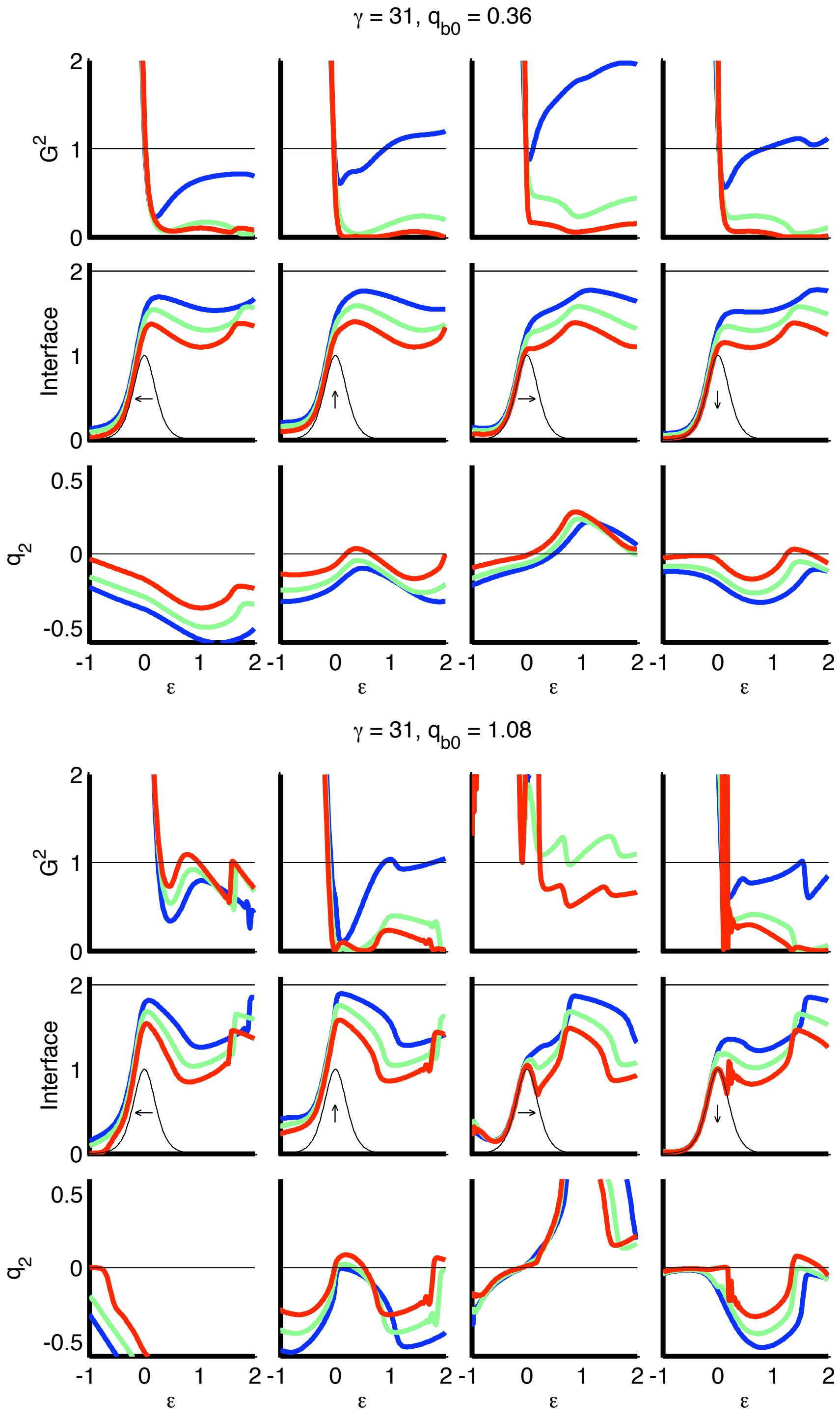

Figure 5.8: The Froude number G^2, the interface, and dense layer transport q_2 at four points through the forcing cycle, at high-$\gamma = 31$ and at three values of h_1 (Blue: $h_1 = 0.37$, Green: $h_1 = 0.56$, Orange: $h_1 = 0.76$), and at two tidal amplitudes ($q_{b0} = 0.36$ - Top, $q_{b0} = 1.08$ - bottom.

over the sill due to the build up of dense water behind the sill. At the end of flood tide, the interface reaches a maximum before the ebb, and the interface at the sill is forced back down. The interface bulge created at the sill at flood tide is emitted downstream during tidal ebb.

q_2, the volumetric transport of dense water over time, reaches a (negative) maximum right of the sill during flood tide. Here, maximum barotropic forcing is accelerating the dense water towards the sill, but not yet interacting with the sill. Once the fluid reaches the sill, beginning at $\zeta = 1$, it begins to reduce the transport, and the dense layer becomes thinner at this point, giving up kinetic energy to build potential energy. Once over the sill crest, the dense transport continues to decline even though its speed is accelerating as the interface thins. Between tidal flood and ebb, q_2 decreases due to decreased forcing. During tidal ebb, barotropic forcing acts opposite to the natural dense layer flow, and reverses the flow right of the sill crest for a period of time, and q_2 becomes positive. This reversal correlates well with the emitted interfacial wave discussed above. As barotropic forcing declines, dense layer transport becomes negative, again building up towards a negative maximum right of the sill.

There are some observable variations between the maximal and sub-maximal flows at this high-γ, low tidal amplitude case. In terms of criticality, sub-maximal flows are similarly supercritical left of the sill crest, and critical at the crest. G^2 right of the sill reaches a maximum during tidal ebb as in the maximal case, but unlike in the maximal case, flow here remains subcritical at all points in the tide. The forcing is not strong enough in this case to create supercritical flow.

The interfaces in the sub-maximal cases act very similar to the maximal case, but lower in the water column. The interface reaches a maximum and minimum at the same times. The amplitude in the interfacial variance is also similar in all cases. One observable difference between sub-maximal and maximal interface developments is that as h_1 increases from maximal to increasingly sub-maximal flows, the wavelength of the internal wave emitted downstream decreases, consonant with the reduced internal wave speed as h_1 thickens. The flow speeds decrease from maximal to sub-maximal flows, thus the wave development is not forced downstream as quickly in these cases.

Studying q_2 in the sub-maximal cases, flows are weaker in general, so q_2 does not reach the values in the sub-maximal case that it does in the maximal flows. Less forcing is necessary to reverse sub-maximal flow, so flow reversal is observed for greater periods of time and larger areas of flow as h_1 increases.

The maximal and sub-maximal flows at high-γ ($\gamma = 31$) is now examined at higher tidal amplitude ($q_{b0} = 1.08$) (Figure 5.8 - Bottom). In general, G^2, the interface, and q_2 react similarly to high amplitude forcing as the low forcing case, but have larger extremes. In terms of G^2, increased forcing during tidal flood periods has a greater effect on sub-maximal flow than in the maximal case. As there is less dense water in these cases, the speeds at which the dense layer is forced over the sill is greater. The increased forcing during tidal ebb causes supercritical flow right of the sill crest in all cases, not only the maximal case as at lower tidal amplitudes. The amplitude of the internal wave observed in the interface plots increases with tidal amplitude, and a large internal bore is forced downstream every tidal cycle. The interface reaches a maximum much closer to the surface of the water column during the flood stage, and reaches a greater depth during ebb flow. During ebb flow in this case the dense flow is completely blocked and reversed everywhere in the dense reservoir.

The same maximal and sub-maximal flows are displayed in the lower-γ case ($\gamma = 9.6$) in order to study the difference between flows of different γ (Figure 5.9). The main observable differences between the two γ examples is in the wavelength and amplitude of the emitted internal waves. At lower γ, either the wave speed is lower or the sill is longer, or potentially both, and the disturbances created at the sill due to the barotropic forcing are not transmitted downstream as quickly as in the high-γ case. Due to the relatively low wave speed and long sill length, the disturbances are not allowed to escape the sill area as quickly as when γ is high, and internal wavelengths of the emitted waves are relatively small. Due to this phenomenon, the disturbance is not able to grow to as great an amplitude in the low-γ case. Even at high tidal forcing, the internal wave amplitude is small in comparison to the high-γ flow.

Time series of q_2 and layer thickness depth y_2 at the sill demonstrates the reproducibility of the results (Figure 5.10). After the initial tidal maximum, each successive tide is approximately equal in both y_2 and q_2. At flood tide, y_2 increases as dense water is forced over the sill crest, and y_2 reaches a minimum during tidal ebb when the forcing is reversed. The transport in the bottom layer q_2 is a maximum.

The progression of y_2 in the sub-maximal flows is similar to the maximal case, but shifted downwards due to the decreased gravitational forcing. The amplitude of change in y_2 also decreases. In the sub-maximal cases, less forcing is needed to reverse dense layer flow at the sill crest. At the same tidal forcing, flow reversal occurs for longer periods during the tidal cycle than in the maximal case. A similar maximum

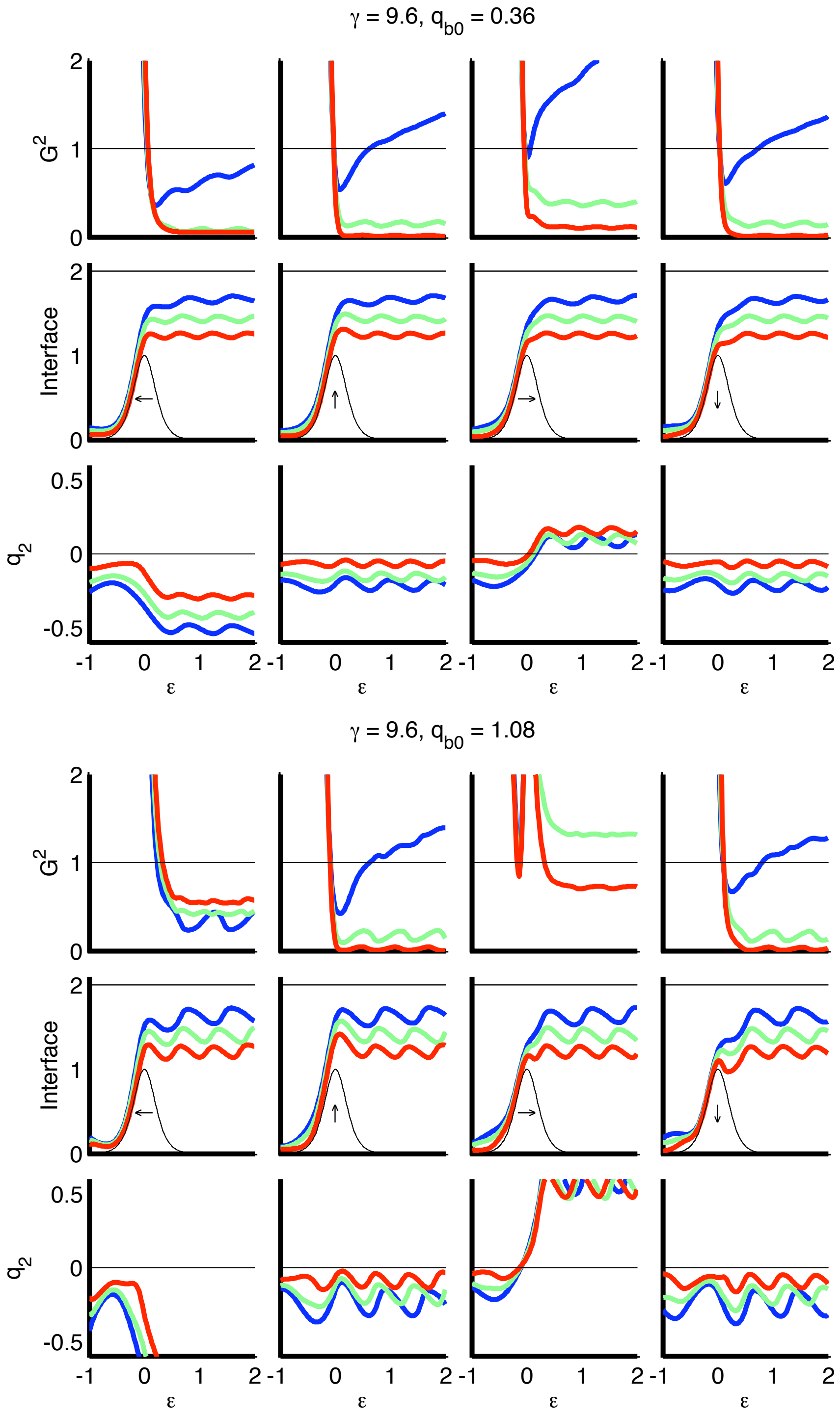

Figure 5.9: The Froude number G^2, the interface, and dense layer transport q_2 at four points through the forcing cycle, at low-$\gamma = 9.6$ and at three values of h_1 (Blue: $h_1 = 0.37$, Green: $h_1 = 0.56$, Orange: $h_1 = 0.76$), and at two tidal amplitudes ($q_{b0} = 0.36$ - Top, $q_{b0} = 1.08$ - bottom.

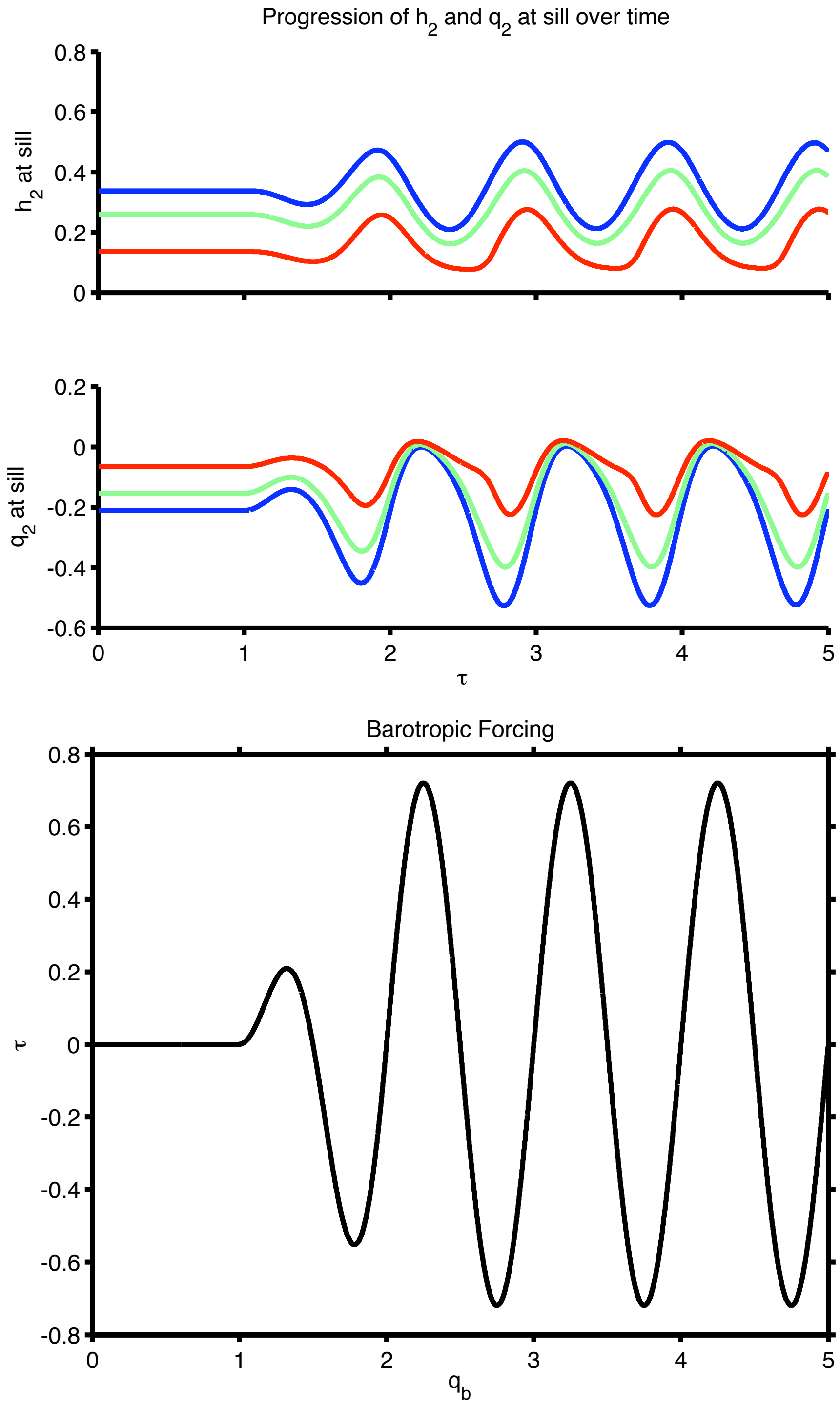

Figure 5.10: Progression of y_2 and q_2 over time at the sill crest (Top), and the barotropic forcing q_b applied (Bottom). Here, $\gamma = 9.6$ and $q_{b0} = 0.72$. Blue: $h_1 = 0.37$, Green: $h_1 = 0.56$, Orange: $h_1 = 0.76$. Exchange rates are calculated over 'normal' tidal cycles, once the model had been fully spun up.

transport q_2 during reversal is observed in the sub-maximal flows as the maximal case. The maximum negative flow during flood tide is not nearly as strong in the sub-maximal cases however, and less dense water is forced over the sill.

5.3.2 Quantifying Barotropically Mediated Exchange

Our problem is governed by four parameters: the interface depth in the dense reservoir h_1, the ratio of the wavespeed to the width for the sill, γ, and the barotropic forcing q_{b0}. The fourth parameter, the height of the sill relative to the reservoir depths is not considered here. We varied h_1 over six values from maximal ($h_1 = 0.3695$) to very sub maximal ($h_1 = 0.7560$), though we did not depress h_1 so far that it was almost at the sill crest ($h_1 \approx 1$).

Descriptions of the relationship between the time-average exchange flow, $< q_i >$, and tidal amplitude q_{b0} show the expected increase in $\langle q_i \rangle / q_{is}$ (Fig. 5.11; where q_{is} is the unforced exchange). There is also a trend for more Sub-maximal runs (red) to have more (normalized) exchange than maximal runs (blue). Easier to see for the Sub-maximal runs (red), there is also a strong dependence on γ, with low γ (stars) having less increase than high γ (circles).

Although trends in the average exchange flow with the three variables mentioned above, a normalization factor that could collapse the results in γ, h_1, or both would help to relate these exchange flows. Subtracting the steady state exchange q_{is} from the time-averaged exchange $< q_i >$ succeeded in collapsing the results in h_1 (Figure 5.12). At each γ, the variation in $(< q_i > - q_{is})$ with h_1 is greatly reduced. For instance, all the stars are quite close together, all the squares, etc. Describing this slight variation, $(< q_i > - q_{is})$ increases inversely with h_1 at each γ.

The γ dependence of the exchange *increase* is relatively well normalized by γ^{-1} (Figure 5.13), with very good agreement for low q_{b0}, and moderately good agreement at stronger forcing. These results indicate that all exchange flows increase at a similar rate with tidal amplitude when normalized by γ. This can help relate all sub-maximal and maximal time-dependent flows.

We now test how these results compare to the maximal quasi-steady prediction. The quasi-steady theory has to be normalized by some coefficient in order to compare to these normalized results. The collapsed result compares fairly well to the maximal quasi-steady prediction when normalized by $\gamma = 60$ (Figure 5.13 - Top).

As tidal amplitude q_{b0} increases, and the system becomes more non-linear in na-

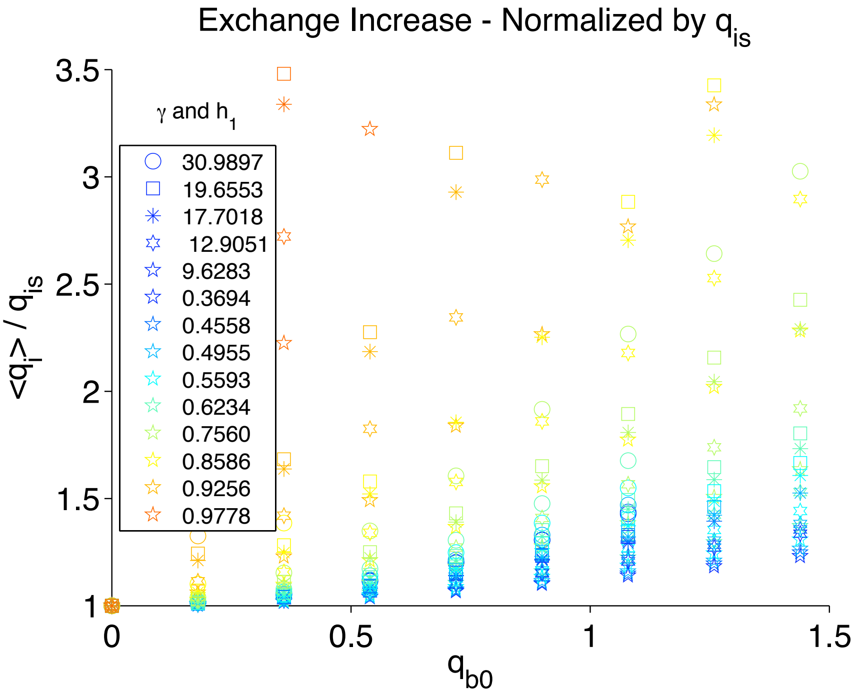

Figure 5.11: Increase in time-averaged exchange flow ($< q_i >$) normalized by the steady exchange case in each case (q_{is}), and plotted against non-dimensional tidal amplitude q_{b0}. Shapes identify different values of γ as indicated in the top half of the legend, and colours differentiate between different h_1s as indicated in the bottom half of the legend.

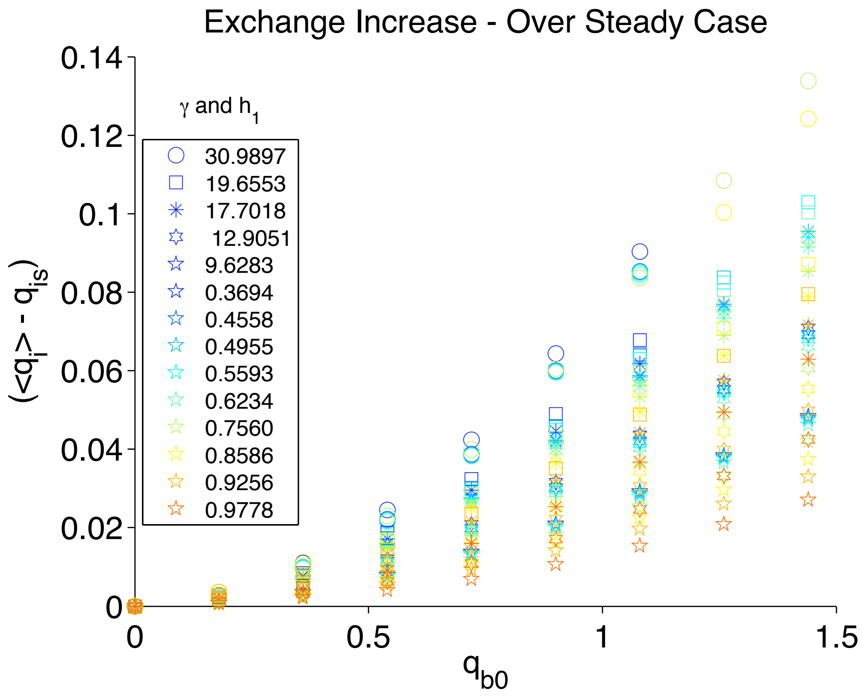

Figure 5.12: Increase in time-averaged exchange flow ($< q_i >$) over the steady exchange case in each case (q_{is}), plotted against non-dimensional tidal amplitude q_{b0}. Shapes identify different values of γ as indicated in the top half of the legend, and colours differentiate between different h_1s as indicated in the bottom half of the legend.

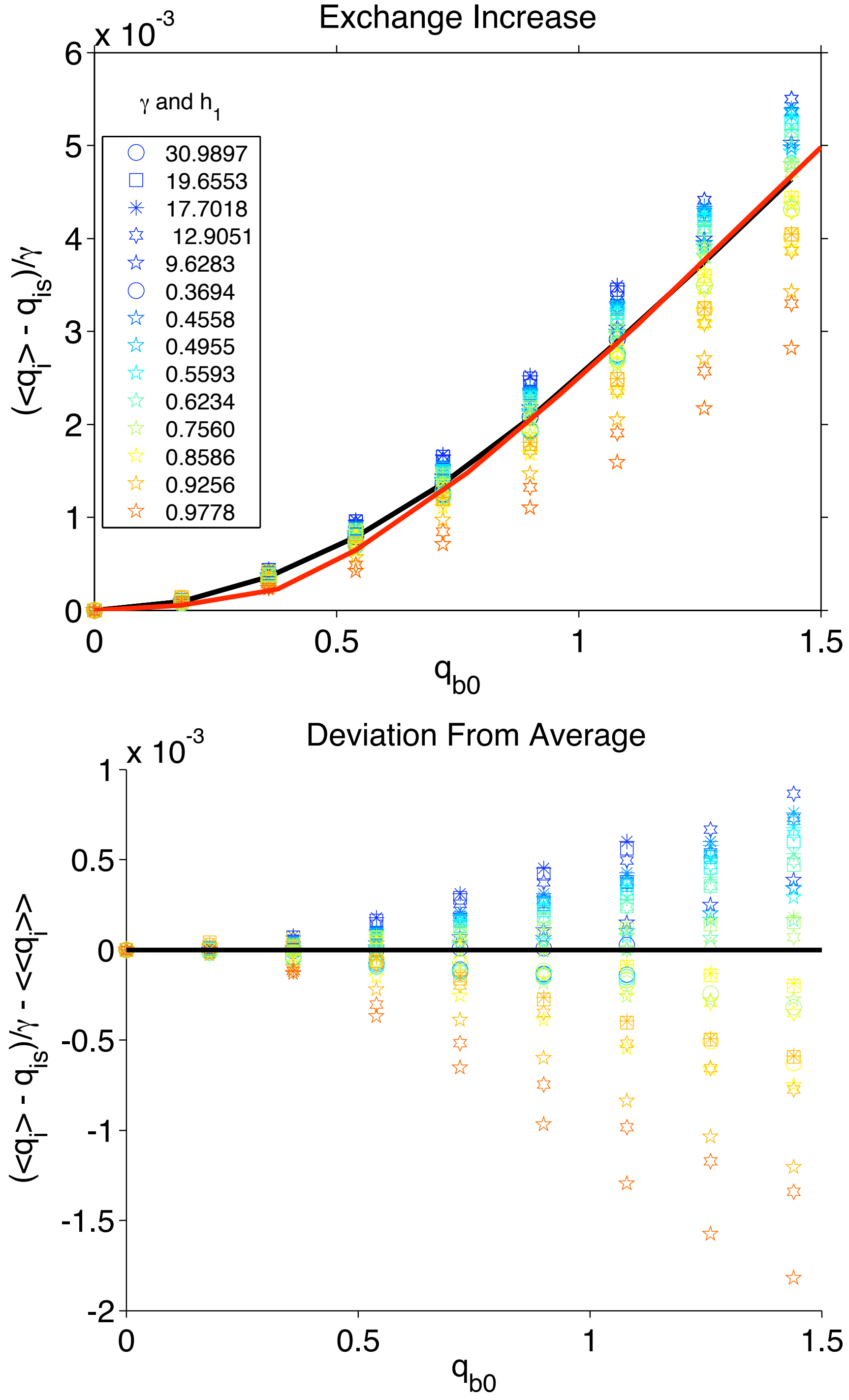

Figure 5.13: The mean result collapses well to the red curve, which is the maximal quasi-steady prediction normalized by a factor of $\gamma = 60$ (Top). The progression of the variability in results is displayed by negating the the progression of the mean solution represented by the thick black line (Bottom). Shapes identify different values of γ as indicated in the top half of the legend, and colours differentiate between different h_1s as indicated in the bottom half of the legend.

ture, the deviations from the normalized result also increases (Figure 5.13). As h_1 increases, and thus the system becomes more sub-maximal, $\frac{<q_i>-q_{is}}{\gamma}$ decreases, a trend that may relate to increased interaction between the interface and the sill. In the extreme case of $h_1 = 0.9778$, the results deviate greatly from the average. At these extreme sub-maximal flows, the normalization factor $\frac{<q_i>-q_{is}}{\gamma}$ does not sufficiently approximate the results. The results at $h_1 \leq 0.9256$, results are fairly consistent.

If normalization $\frac{<q_i>-q_{is}}{\gamma}$ related all exchange flows perfectly at any given q_{b0}, changes in γ and h_1 would not change $\frac{<q_i>-q_{is}}{\gamma}$. Results show this is not the case (Figure 5.14). At high and low γ, $\frac{<q_i>-q_{is}}{\gamma}$ is noticeably smaller than at the other examples, so the normalization does not apply as well at these extremes. Additionally, at $h_1 > 0.8586$, the normalization is not as accurate as $\frac{<q_i>-q_{is}}{\gamma}$ decreases significantly in all cases. Results deviate somewhat in the maximal case as well, but to a smaller degree.

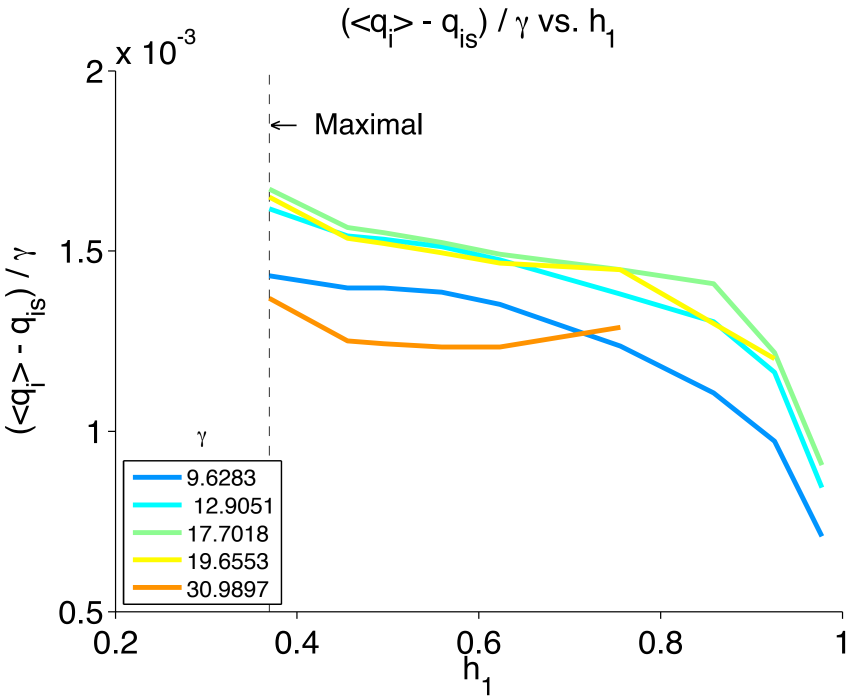

Figure 5.14: Figure 1: Normalized exchange flow plotted against h_1 where $q_{b0} = 0.72$. High and low-γ values are lower than the moderate cases. At $\gamma = 13, 17.7$ and 19.7, results are similar.

Although $\frac{<q_i>-q_{is}}{\gamma}$ is not stable in h_1 and γ, stability is approached between $\gamma = 13$ and 19.7, where $\frac{<q_i>-q_{is}}{\gamma}$ decreases only slightly from $h_1 = 0.4558$ to $h_1 = 0.8586$.

Thus variation in $\frac{<q_i>-q_{is}}{\gamma}$ in this span can largely be ignored.

The relationship between q_{is} and h_1 is now investigated (Figure 5.15). q_{is} is steady in γ, thus only changes with h_1. The relationship between q_{is} and h_1 is approximately linear from $h_1 \approx 0.5$ to $h_1 \approx 0.85$. This is the same range where $\frac{<q_i>-q_{is}}{\gamma}$ is most stable (Figure 5.14), and may explain the deviation of $\frac{<q_i>-q_{is}}{\gamma}$ from stability outside this range.

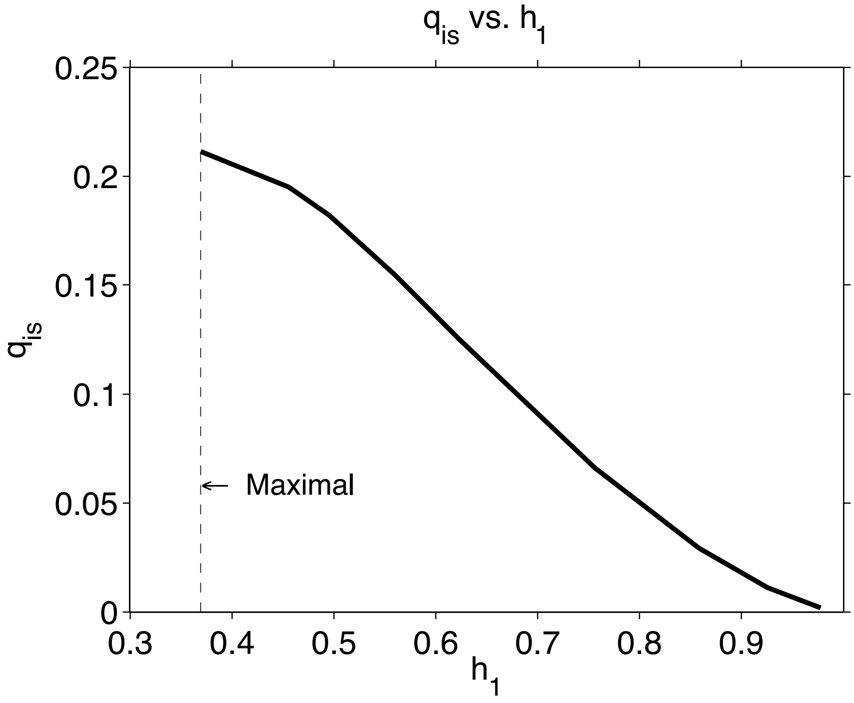

Figure 5.15: Steady state transport q_{is} vs. h_1. q_{is} is steady with γ, so this result applies in all cases.

The high-γ and low-γ cases have a lower average $\frac{<q_i>-q_{is}}{\gamma}$ than the moderate γ examples (Figure 5.13). As $\frac{<q_i>}{q_{is}}$ approaches the quasi-steady solution, the variation in $< q_i >$ with γ decreases. Using γ to normalize results therefore should not collapse as this limit is approached. Similarly, as $\gamma \rightarrow 0$, $< q_i >$ would cease to react to tidal forcing. Thus at both the very high-γ and low-γ limits, results should deviate from the average trend represented by these results.

In order to build towards an applicable interpretation of the results, it is useful to define the shape of the collapsed curve. It was previously understood using quasi-steady theory that as q_{b0} increased, $< q_i >$ would approach a straight line of slope π^{-1} (Farmer and Armi, 1986). Studying the collapsed $\frac{<q_i>-q_{is}}{\gamma}$ curve, it was determined that as q_{b0} increases, $\frac{<q_i>-q_{is}}{\gamma}$ approaches a straight line of slope $(65\pi)^{-1}$ (Figure 5.16). This slope could be applied to extend the average result to greater q_{b0} values in addition to helping define the shape of the curve.

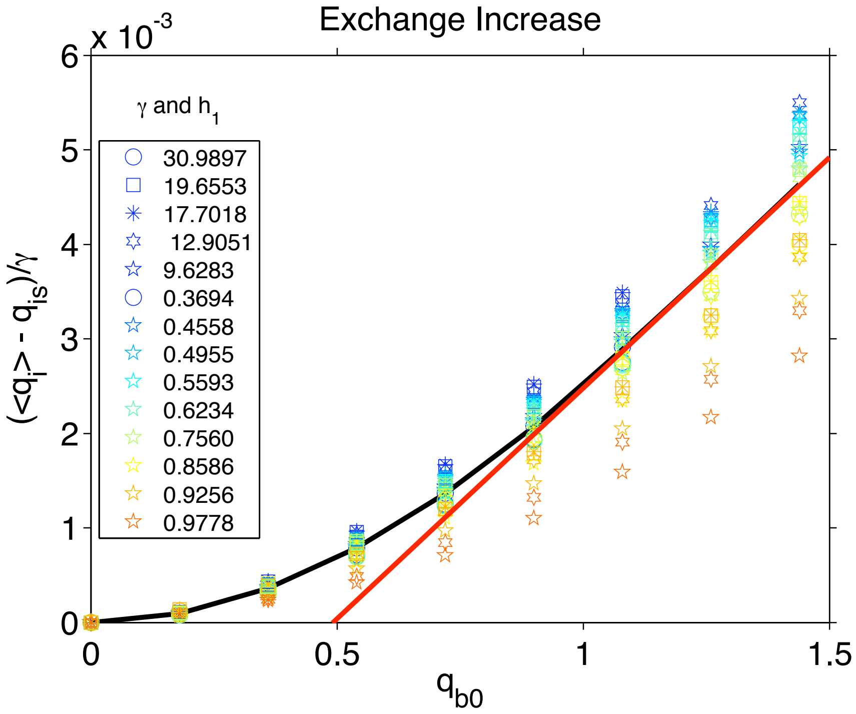

Figure 5.16: $\frac{<q_i>-q_{is}}{\gamma}$ on average tend to a line of slope $\frac{1}{65\pi}$, represented here by the red line. The thick black line represents the progression of the mean solution. Shapes identify different values of γ as indicated in the top half of the legend, and colours differentiate between different h_1s as indicated in the bottom half of the legend.

Chapter 6

Summary and Discussion

We have found that the time-averaged exchange flows increase at a similar rate due to tidal forcing when normalized by the non-dimensional parameter γ. This result relates most time-dependent sub-maximal regimes in with the maximal flow, although as $h_1 \to 1$, results deviate from this mean. This will help to simplify the problem of modeling these flows and the related strait dynamics world-wide, as all flows are independent in terms of parameter space, yet related through this approximation.

The modeling and predictability of exchange flow is applicable to various areas of interest in addition to the potential use in improving climate modeling discussed previously. Biologically, growth in the surrounding waters is affected by the nature of the flow, as it influences the nutrient and pollutant transport. For this reason, water quality and properties such as anoxia can be dependent on the nature of the exchange. Transportation of energy also depends on this flow, and resultant effects such as internal waves can influence basin mixing. With so many important influences, it would be valuable to quantitatively and accurately predict the nature of these flows.

Steady hydraulic theory traditionally applied to exchange flows has been extended to include barotropic forcing and time dependence in the sub-maximal case. Previous research on the time-dependent maximal case (Helfrich, 1995) was duplicated and extended to include sub-maximal exchange. Maximal results depend on two parameters, γ (4), which differentiates between sill geometry and wave speeds in the strait, and q_{b0} (26), the tidal amplitude. h_1,which determines the strength of the flow without barotropic forcing, was added here as a third parameter to differentiate between sub-maximal flows.

We tested the applicability of parameter γ. An infinite number of different strait geometries could theoretically have the same γ, and for γ to be generally applicable, the exchange flows in each of these cases would have to be the same, and react the same to tidal forcing. Five flows of $\gamma = 21.844$ are studied, with g' and L varying between each case. The resultant time-averaged exchange flows in each case were the same, proving γ to be applicable in the sill controlled case. Past results have shown results of the same γ to vary in the offset sill-narrows case (Helfrich, 1995), a flow that is not considered in this study.

The progression of the time-averaged exchange flow with changes in the three parameters above is the focus of this study. At a given h_1 and γ, the average exchange flow increases with q_{b0}. This means that tidal forcing always increases the time-averaged exchange flow.

At a fixed q_{b0} and h_1, the average exchange flow was found to increase with γ, thus the exchange in straits with dynamically short sills and fast wave speeds reacts more to tidal forcing than those with longer sills or slower wave speeds. Short sills and fast wave speeds allow internal waves developed due to tidal forcing to escape the immediate area of the sill, and allows the exchange to react without negative effects of these waves. This result was known previously in the maximal case, and here is found also to be true for sub-maximal flows.

Fixing γ and q_{b0}, the average exchange development with h_1 needed to be normalized in order to compare results in a useful manner. As h_1 varies, so too does the exchange with no forcing, q_{is}. To properly compare the role of the tides on these flows, we found it adequate to subtract q_{is} from $\langle q_i \rangle$, and found that $(< q_i > -q_{is})$ is approximately the same for all h_1 studied, with a slight increase as h_1 decreases (Figure 5.12). Thus, at each γ, tidal forcing increases the average exchange at a similar rate at each h_1 value for the moderate range of maximal $< h_1 < 0.93$ considered here. At the more extreme case of $h_1 = 0.98$, where results deviated from this range.

Our overall normalization of the exchange increase by γ largely collapses the response of the three dimensions in this parameter space to a single dimension $(< q_i > -q_{is})/\gamma$ governed by q_{b0}. This collapse is not perfect, but the deviation from the general trend is about 10% for maximal $< h_1 < 0.93$. The average curve approaches a line of slope $(65\pi)^{-1}$, as predicted from quasi-steady theory (Farmer and Armi,1986).

The results found assume that factors neglected do not appreciably affect the the modeled results. The definition of the strait geometry is highly simplified. Simplifying the problem into two layers is unrealistic, but was adopted here in order to simplify the problem to study the effect of barotropic forcing on sub-maximal exchange flows. Bottom friction may act to shift the modeled exchange towards the sub-maximal.

Inter-layer friction has also been neglected. The hydrostatic nature of this model may have acted to neglect potentially important wave features such as resonant and solitary waves that may be present in real life examples of these flows (Helfrich, 1995). However, the model does allow for resultant internal waves to be emitted which relate to the creation of these features. Even though some resultant internal waves may not be accurately modeled here, the effect that these waves would have on the average exchange flow is minimal. Numerically describing the effects these factors have on the modeled results would be a valuable step towards accurately predicting these exchange flows.

We have left some of the natural parameter space of even this simplified physics problem unexplored. For $h_1 > 1.0$ there is no mean exchange flow and the dense layer is completely blocked in the unforced case from spilling over the sill. If h_1 and γ are not too large, then the barotropic flow can lift the dense layer over the sill and drive an exchange flow in the tidally forced case, a process we have not explored here. Secondly, we have not explored extremes in the basin depths relative to the sill depth. If the basins are very deep, the results will not change very much as interfacial wave speeds will be based solely on the surface layer thickness. However, if the basins are shallow, there is the possibility that the reservoir conditions will flood the control and change the physics of the problem. These cases have been avoided here.

Bibliography

[1] Armi, L. (1986), The hydraulics of two flowing layers with different densities, Journal of Fluid Mechanics, 163, 27-58

[2] Armi, L. & D.M. Farmer (1986), Maximal two-layer exchange through a contraction with barotropic net flow, Journal of Fluid Mechanics, 164, 27-51

[3] Baines, P.G. (1995) Topographic Effects in Stratified Flows. New York: Cambridge University Press.

[4] Bray, N.A., J. Ochoa, & T.H. Kinder (1995), The role of the interface in exchange through the Strait of Gibraltar, Jornal of Geophysical Research-Oceans, 100 (C6), 10755-10776

[5] Farmer, D.M. & L. Armi (1986), Maximal two-layer exchange over a sill & through the combination of a sill and contraction with barotropic flow, Journal of Fluid Mechanics, 164, 53-76

[6] Frankcombe, L.M. & A.McC. Hogg (2007), Tidal modulation of two-layer hydraulic exchange flows, Ocean Science, 3, 179-188

[7] Gregg, M.C. & E. Özsoy (2002), Flow, water mass changes, and hydraulics in the Bosphorus, Journal of Geophysical Research, 107, 2-1 - 2-23

[8] Helfrich, K.R. (1995), Time-Dependent Two-Layer Hydraulic Exchange Flows*, Journal of Physical Oceanography, 25, 359-373

[9] Ivey, G.N. (2004), Stratification and mixing in sea straits, Deep-Sea Research II, 51, 441-453

[10] Klymak, J.M., & M.C. Gregg (2003), The Role of Upstream Waves and a Downstream Density Pool in the Growth of Lee Waves: Stratified Flow over the Knight Inlet Sill, Journal of Physical Oceanography, 33, 1446-1461

[11] Manning, C.C., R.C. Hamme, & A. Bourbonnais (2010), Impact of deep-water renewal events on fixed nitrogen loss from seasonally-anoxic Saanich Inlet, Marine Chemistry, 122, 1-10

[12] Marshall, J., C. Hill, L. Perelman, & A. Adcroft (1997), Hydrostatic, quasi-hydrostatic, and nonhydrostatic ocean modeling, Journal of Geophysical Research, 102, C3, 5733-5752

[13] Pratt, L.J., W. Johns, S.P. Murray, & K. Katsumata (1999), Hydraulic interpretation of direct velocity measurements in the Bab al Mandab, Journal of Physical Oceanography, 29 (11), 2769 - 2784

[14] Valle-Levinson, A. (2008), Density-driven exchange flow in terms of the Kelvin and Ekman numbers, Journal of Geophysical Research, 113, C04001

[15] Wesson, J.C. & M.C. Gregg (1994), Mixing at Carmarinal Sill in the Strait of Gibraltar, Journal of Geophysical Research, 99, 9847-9878

[16] Winters, K.B. & H.E. Seim (2000), The role of dissipation and mixing in exchange flow through a contracting channel, Journal of Fluid Mechanics, 407, 265-290

Appendix A

Additional Information

h_1	Used to describe steady state thickness of top layer for given runs to differentiate between initial conditions
$\gamma = \frac{(g'H)^{\frac{1}{2}}T}{L}$	Non-dimensional parameter
$< q_i >$	Time-averaged exchange flow
q_{is}	Steady state exchange flow for a given γ and h_1
$q_{b0} = \frac{u_{b0}}{(g'H)^{\frac{1}{2}}}$	Non-dimensional barotropic tidal amplitude
$q_r = \frac{q_1}{-q_2}$	Fractional Exchange flow at sill crest
$g' = \frac{g\Delta\rho}{\rho_2}$	Reduced gravitational acceleration
$F_i = \frac{u_i}{\sqrt{g'y_i}}$	Dimensionless Froude Number for each layer
$G^2 = F_1^2 + F_2^2 = \frac{u_1^2}{g'y_1} + \frac{u_2^2}{g'y_2}$	Composite Froude Number
y_i	Layer thickness ($i = 1$ is the top layer)
H	Water thickness above sill crest
T	Tidal period
u_i	Layer velocity
ρ_i	Layer density
u_{b0}	Imposed barotropic tidal velocity amplitude